

The Statistics of Density Peaks and the Column Density Distribution of the Lyman-Alpha Forest

Lam Hui^{1,2,5}, Nickolay Y. Gnedin^{1,3,6} and Yu Zhang⁴

ABSTRACT

We develop a method to calculate the column density distribution of the Ly α forest for column densities in the range $10^{12.5} - 10^{14.5} \text{ cm}^{-2}$. The Zel'dovich approximation, with appropriate smoothing, is used to compute the density and peculiar velocity fields. The effect of the latter on absorption profiles is discussed and it is shown to have little effect on the column density distribution. An approximation is introduced in which the column density distribution is related to a statistic of density peaks (involving its height and first and second derivatives along the line of sight) in real space. We show that the slope of the column density distribution is determined by the temperature-density relation as well as the power spectrum on scales $2 \text{ hMpc}^{-1} \lesssim k \lesssim 20 \text{ hMpc}^{-1}$. An expression relating the three is given. We find very good agreement between the column density distribution obtained by applying the Voigt-profile-fitting technique to the output of a full hydrodynamic simulation and that obtained using our approximate method for a test model. This formalism then is applied to study a group of CDM as well as CHDM models. We show that the amplitude of the column density distribution depends on the combination of parameters $(\Omega_b h^2)^2 T_0^{-0.7} J_{\text{HI}}^{-1}$, which is not well-constrained by independent observations. The slope of the distribution, on the other hand, can be used to distinguish between different models: those with a smaller amplitude and a steeper slope of the power spectrum on small scales give rise to steeper distributions, for the

¹Department of Physics, Massachusetts Institute of Technology, Cambridge, MA 02139

²Center for Theoretical Physics, Laboratory for Nuclear Science, MIT

³Princeton University Observatory, Peyton Hall, Princeton, NJ 08544

⁴Laboratory for Computational Astrophysics, National Center for Supercomputing Applications, University of Illinois at Urbana-Champaign, Urbana, IL 61801

⁵Present Address: NASA/Fermilab Astrophysics Center, Fermi National Accelerator Laboratory, Batavia, IL 60510; e-mail: *lhui@hydra.fnal.gov*

⁶Present Address: Department of Astronomy, University of California, Berkeley, CA 94720

range of column densities we study. Comparison with high resolution Keck data is made.

Subject headings: cosmology: theory — intergalactic medium — quasars: absorption lines

1. Introduction

There is a long history of theoretical efforts to place the study of the Ly α forest within the framework of cosmological structure formation theories (Doroshkevich & Shandarin 1977; Rees 1986; Bond, Szalay & Silk 1988; McGill 1990; Bi, Börner & Chu 1992). Recent work making use of numerical simulations has greatly advanced our understanding in this direction (Cen et al. 1994; Zhang, Anninos & Norman 1995; Hernquist et al. 1995; Petitjean, Mücke & Kates 1995; Miralda-Escudé et al. 1996). (See also Bi, Ge & Fang 1995, for a linear theory calculation). The emerging picture is that it is possible to account for all the observed properties of the Ly α forest (with column densities less than about 10^{17} cm^{-2}) by assuming it originates from the small scale structure, including the network of filaments, pancakes and mild density fluctuations, which arises naturally in hierarchical clustering cosmological models (Weinberg et al. 1996).

A commonly used statistic to characterize the forest is its column density distribution, the number of absorption lines per unit neutral hydrogen column density per unit redshift as a function of column density. Other useful statistics include line-line correlations and the distributions of b -values and equivalent widths (Murdoch et al. 1986; Carswell et al. 1991; Press, Rybicki & Schneider 1993; Crisitani et al. 1995). There have also been proposals of new statistical tools (Meiksin and Bouchet 1995; Miralda-Escudé et al. 1996; Pando and Fang 1996). (See Tytler 1992 for a general overview of the statistical issues concerning quasar absorption systems.) We focus our attention on the column density distribution in the present work.

One of the most striking features of the observed column density distribution of quasar absorption systems is that it can be approximated by a single power law that extends over many orders of magnitude. This was emphasized by Tytler (1987), among others, who found that in the range $10^{13} < N_{\text{HI}} < 10^{22} \text{ cm}^{-2}$, the distribution was reasonably well represented by a power law, $\propto N_{\text{HI}}^{-\beta}$ with $\beta = 1.51 \pm 0.02$. However, there exists evidence of at least one break. It has been demonstrated that there is a deficit of absorption systems somewhere in the column density range 10^{14} to 10^{17} cm^{-2} compared to a power-law extrapolation of the distribution from lower column densities (Carswell et al. 1987; Petitjean et al. 1993;

Hu et al. 1995; Giallongo et al. 1996). For reasons that have to do with the nature of the approximations that we make (Sec. 5.2), we focus our attention on absorption systems with column densities in the range $10^{12.5} < N_{\text{HI}} < 10^{14.5} \text{ cm}^{-2}$. Hu et al. (1995) obtained $\beta = 1.46$ with a 95% confidence range of (1.37, 1.51) in the column density range $10^{12.3} < N_{\text{HI}} < 10^{14.5} \text{ cm}^{-2}$. Lu et al. (1996) found the same best-fit β for the same range of column densities.

An obvious ultimate goal of recent theoretical work on the Ly α forest is to constrain theories of structure formation. The natural question is: what determines the normalization and slope of the column density distribution? What are the major determining factors, in addition to the usual parameters specified by a given cosmological model? To answer these questions, another question has to be addressed: what are the analytical and/or computational tools necessary to make accurate predictions for the column density distribution, given all the required parameters?

Accordingly, the present work can be divided into three parts, where the tools are developed, the factors that influence the column density distribution are analyzed and one application to a class of cosmological models is discussed.

Numerical hydrodynamic simulations (Cen et al. 1994; Zhang et al. 1995; Hernquist et al. 1995; Miralda-Escudé et al. 1996) provide the most obvious tools to study the Ly α forest. Computational costs, however, prevent one from testing extensively several cosmological models. We show in this paper that the Zel'dovich approximation (Zel'dovich 1970), with appropriate smoothing, is an efficient and accurate alternative (see also Doroshkevich & Shandarin 1977). Our basic assumption is that the part of the Ly α forest with column densities less than about $10^{14.5} \text{ cm}^{-2}$ arises mostly from regions which are slightly overdense (overdensity $\lesssim 5$) or even underdense and which have not undergone orbit-crossing. The Zel'dovich approximation can then be coupled with the equations governing the thermal and ionization states of the gas to yield accurate predictions for the density of neutral hydrogen and the peculiar velocity as a function of position. Absorption spectra are then generated and analyzed. Basic expressions for the absorption optical depth are presented in Sec. 2 and the approximations that go into its computation are discussed in Sec. 3.

Given an absorption spectrum, the column density distribution depends on the method of identifying lines and assigning column densities. This is discussed in Sec. 4.1. We investigate the effects of peculiar velocities on the column density distribution, using a method described by Miralda-Escudé (1996). We find that although peculiar velocities can strongly influence the shapes of absorption profiles, they play a relatively minor role in determining the column density distribution. The various interesting effects of peculiar velocities are discussed in Sec. 4.2. Motivated by this finding, a very different way of

assigning column densities is introduced in Sec. 5, in which no absorption spectrum needs to be generated. In the absence of peculiar velocities, there is a one-to-one correspondence between density peaks in real space (if they are separated by a distance larger than a minimum corresponding to the thermal broadening width) and minima of transmission (maxima in absorption) in the observed spectrum. Under such conditions, we can simply associate each density peak in real space with an absorption line and assign a column density to each based on the height and curvature of the peak. The column density distribution is then a statistic of density peaks in real space. We apply this procedure (we call it the Density-Peak-Ansatz) to the density field predicted by the truncated Zel'dovich approximation and test the result against that of a full hydrodynamic simulation. The column density distribution obtained in this way is compared to that obtained from the hydrodynamic simulation using the Voigt-profile-fitting-technique, which is the line-identification method most widely used. The level of agreement is found to be excellent. In Sec. 5.2, we discuss the range of parameters in which our computed column density distribution is expected to be reliable.

Armed with the right tools, we turn our attention to the second question: what factors determine the column density distribution? They can be divided into two categories. One has to do with properties of the intergalactic medium, including its temperature, the equation of state (or temperature-density relation, which we will use interchangeably; see Hui & Gnedin 1996), the ionizing radiation intensity and the baryon density. Uncertainties in all of them have to be taken into account before one can meaningfully confront theories with observations. We distinguish between the factors that mostly affect the normalization of the column density distribution and those that mostly affect its slope. It is found that the temperature-density relation (weakly) affects the slope while the rest of the above factors influences the normalization. It is also emphasized that the temperature and the equation of state depend on the reionization history of the universe (a fuller discussion of this point and related topics will be given in a separate paper). The second set of factors affecting the column density distribution has to do with the specific cosmological model, namely the normalization and shape of the corresponding power spectrum. We study a few variants of the Cold Dark Matter (CDM) model in Sec. 7 for this purpose. It is found that the amplitude and slope of the linear power spectrum on comoving scales of around $2 h \text{ Mpc}^{-1}$ to $20 h \text{ Mpc}^{-1}$ are the most important factors in determining the slope of the column density distribution (the equation of state also has a weak effect on it). Decreasing the amplitude and/or steepening the slope of the power spectrum tends to steepen the distribution in the column density range about $10^{12.5}$ to $10^{14.5} \text{ cm}^{-2}$. We introduce an expression relating the slope of the column density distribution to the equation of state and properties of the power spectrum on small scales.

We then study a class of Cold plus Hot Dark Matter (CHDM) models in Sec. 8, making use of the insights gained in Sec. 6 and Sec. 7. The $\Omega_\nu = 0.2$ (density parameter in neutrino) models have steeper column density distributions compared to those with $\Omega_\nu = 0.1$ because they have less power on the relevant scales. In particular, the low Hubble constant ($H_0 = 50 \text{ km s}^{-1} \text{ Mpc}^{-1}$) $\Omega_\nu = 0.2$ models predict slopes that are steeper than the observed one for most of the parameter-space specifying the properties of the intergalactic medium. Only for equations of state that are close to isothermal can the two be made consistent with each other. We emphasize however that a more detailed comparison between the models and observations, taking fully into account instrumental noise and biases of the line-identification method(s), is necessary before one can firmly reject any model. We conclude in Sec. 9 .

It is appropriate that we mention here two recent pieces of work along similar lines as described above, but using a different dynamical approximation, namely the lognormal approximation: Bi & Davidsen (1997) and Gnedin & Hui (1996). The former, in particular, contains a very comprehensive and careful analysis of the many different observational properties of the Ly α forest. One strong point of their analysis is that they tested their method using VPFIT, a spectral analysis routine that is commonly used by observers. We will discuss the predictions for the column density distribution by the lognormal and the Zel'dovich approximations in Sec. 5.

In our notation, bold faced letters are reserved for three-dimensional vectors. The symbols \mathbf{v}_{pec} and \mathbf{x} denote the three-dimensional peculiar velocity and comoving position while v_{pec} and x are their counterparts along the line of sight of interest. Standard symbols are used for cosmological parameters: H for the Hubble constant as a function of z , H_0 for the Hubble constant today, h for $H_0/100 \text{ km s}^{-1} \text{ Mpc}^{-1}$, Ω_0 for the density parameter today, with the subscript b to denote its baryon portion and ν its neutrino content. We use the symbol h (as distinct from h) to denote the Planck constant in a few places where it arises. The term multiple-streaming is reserved for the situation where a single observed redshift corresponds to more than one position in real space. We distinguish it from the term orbit-crossing, which is commonly used interchangeably with multiple-streaming in other contexts. Orbit-crossing refers to the case where a single position has more than one velocity.

2. Cosmological Lyman-Alpha Absorption in a Fluctuating Medium: Basic Results

A photon emitted with energy higher than 10.196 eV (wavelength of 1216 \AA) by a distant quasar is continuously redshifted as it travels through the intergalactic medium until it reaches the observer. At some intermediate point, the photon is redshifted to around 1216 \AA in the rest frame of the intervening medium, which may contain neutral hydrogen. It can then excite the $\text{Ly}\alpha$ transition and be absorbed. Let us consider a particular line of sight from the observer to the quasar. The optical depth τ (the probability of transmission is given by $e^{-\tau}$) of a photon at a given observed frequency ν_o is given by:

$$\tau(\nu_o) = \int_{x_A}^{x_B} n_{\text{HI}} \sigma_\alpha \frac{dx}{1+z}, \quad (1)$$

where x is the comoving radial coordinate of some intermediate point along the line of sight, z is the redshift and n_{HI} is the proper number density of neutral hydrogen at that point. The limits of integration, x_A and x_B , are the comoving positions of the observer and the quasar. The $\text{Ly}\alpha$ absorption cross-section is denoted by σ_α . It is a function of the frequency of the photon with respect to the rest frame of the intervening hydrogen at position x . Let us call this frequency ν . The cross-section is peaked when ν is equal to the $\text{Ly}\alpha$ frequency, ν_α .

The frequency ν is related to the observed frequency ν_o by:

$$\nu = \nu_o (1+z) \left(1 + \frac{v_{\text{pec}}}{c} \right), \quad (2)$$

where v_{pec} is the peculiar velocity along the line of sight at position x and $1+z$ is the redshift factor *due to the uniform Hubble expansion alone* at the same position. The peculiar velocity of the observer, which merely displaces the whole spectrum by a constant amount (independent of x), is ignored. The quantity v_{pec}/c , where c is the speed of light, is much smaller than 1.

It proves convenient for later discussion to expand z around some mean redshift of interest \bar{z} , which could be the redshift of a simulation output or the average redshift of an observed spectrum with limited redshift range. Using $dx = cdt/a$, where a is the Hubble scale factor and t is the proper time, it can be shown that

$$\nu = \nu_o (1+\bar{z}) \left(1 + \frac{u}{c} \right), \quad u \equiv \frac{\bar{H}}{1+\bar{z}} (x - \bar{x}) + v_{\text{pec}}(x), \quad (3)$$

where \bar{x} is the position at which the redshift due to Hubble expansion coincides exactly with \bar{z} . The Hubble constant at the same redshift is denoted by \bar{H} . We assume the range of x is small enough so that $u/c \ll 1$. The convention $a = 1$ today is adopted.

The velocity coordinate u defined above contains contributions from both the Hubble expansion and the peculiar motion. Without peculiar motion, u increases monotonically with x and is in fact linear in x . Peculiar velocities destroy the linear relation and could give rise to situations where a given u corresponds to more than one position x . It implies that a photon of a given observed frequency ν_o can have the same rest-frame frequency ν at more than one place in its trajectory from the quasar to the observer. We reserve the term multiple-streaming to this situation and distinguish it from orbit-crossing where a given x carries more than one v_{pec} or u . We will return to the subject of multiple-streaming in Sec. 4.2 and that of orbit-crossing in Sec. 3.1.

We define one more velocity coordinate u_o , which is related to the observed frequency ν_o by:

$$\nu_o = \frac{\nu_\alpha}{1 + \bar{z}} \left(1 - \frac{u_o}{c} \right) \quad (4)$$

where ν_α is the Ly α frequency. The velocity coordinate u_o is simply equal to u when ν coincides exactly with ν_α (this can be seen by comparing eq. [3] and [4], bearing in mind that u/c and u_o/c are both assumed to be much less than 1).

With the definitions in place, we change the variable from x to u in equation (1), which results in the following expression for τ , now a function of u_o :

$$\tau(u_o) = \sum \int_{u_A}^{u_B} \frac{n_{\text{HI}}}{1 + z} \left| \frac{du}{dx} \right|^{-1} \sigma_\alpha du, \quad \sigma_\alpha = \sigma_{\alpha 0} \frac{c}{b\sqrt{\pi}} e^{-(u - u_o)^2/b^2}. \quad (5)$$

The summation refers to a sum over multiple-streams (all the x 's within the range $x_A - x_B$ that corresponds to a given u), and n_{HI} , z and $|du/dx|^{-1}$ are now functions of u . The limits of integration u_A and u_B are the velocity coordinates corresponding to the positions x_A and x_B (assuming no orbit-crossing so that each x carries one u). Note that in practice, only a limited range of u contributes to τ for a limited range of u_o so that one can replace the redshift z with \bar{z} . The same is also true for equation (1).

The Ly α cross-section is expressed as a function of $u - u_o$. The constant $\sigma_{\alpha 0}$ is equal to the combination of fundamental physical constants $0.416\pi q^2/(m_e c \nu_\alpha)$, where q is the charge of an electron and m_e is its mass. It is about $4.5 \times 10^{-18} \text{ cm}^2$. The parameter b is equal to $\sqrt{2k_B T/m_p}$ where k_B is the Boltzmann constant, m_p is the mass of a proton and T is the temperature of the gas at the velocity coordinate u .

The form of the line profile function above takes into account thermal broadening but ignores the natural line width. A more general profile function involves a convolution of the two, resulting in the Voigt profile (Rybicki & Lightman 1979). However, the Voigt profiles are accurately thermal profiles for column density less than about 10^{17} cm^{-2} . The reader is

referred to Spitzer (1978) and Press and Rybicki (1993) for discussions of curve of growth analysis.

Note also that it is sometimes assumed b contains a component due to turbulent motion. We do not include it explicitly in our formalism. Bulk motion, on the other hand, is accounted for by v_{pec} or u .

Let us consider two different limits of equation (5).

Suppose there is a high local maximum in $n_{\text{HI}}|du/dx|^{-1}$ at some $u = u_{\text{max}}$ with width in velocity space much smaller than the thermal width b . Then one can take the line profile function associated with σ_{α} out of the integral in equation (5) because $n_{\text{HI}}|du/dx|^{-1}$ varies much more rapidly than the thermal profile:

$$\tau(u_{\circ}) = \left(\int_{\text{max}} n_{\text{HI}}(x) \frac{dx}{1+z} \right) \sigma_{\alpha 0} \frac{c}{b\sqrt{\pi}} e^{-(u_{\circ} - u_{\text{max}})^2/b^2}, \quad (6)$$

where the variable of integration has been changed back from u to x . The equation holds when u_{\circ} is close enough to u_{max} . The integral is over the local maximum, assuming that the amount of neutral hydrogen away from the maximum does not cause significant absorption (until another maximum is encountered). One then sees an absorption line with a Gaussian profile in optical depth. While the width of the line tells us about b , which is proportional to the square root of the temperature, the depth of the line provides information about both b and the column density, which is the integral inside the first pair of brackets on the right hand side. Let us call this the narrow-maximum-limit.

Consider another limit of the integral (eq. [5]) in which $n_{\text{HI}}|du/dx|^{-1}$ varies slowly with u . Suppose the scale of variation is much larger than the thermal width. In this case, one can leave the line profile function inside the integral but take the rest outside:⁷

$$\tau(u_{\circ}) = \sum \frac{n_{\text{HI}}}{1+\bar{z}} \left| \frac{du}{dx} \right|^{-1} c \sigma_{\alpha 0}. \quad (7)$$

The velocity dependent terms on the right hand side are evaluated at u_{\circ} . The profile function has been integrated out.

In the above limit, τ does not necessarily have the thermal profile around its maxima. We will call this the broad-maximum-limit. An extreme example is that of a homogeneous medium, which gives rise to featureless and uniform absorption (Gunn & Peterson 1965).

⁷The expression is not valid at velocity caustics, where du/dx vanishes. Further discussion on velocity caustics can be found in Sec. 4.2.

Conventional analysis of quasar spectra involves identifying those parts of the spectra that are due to the Ly α absorption and fitting them with superpositions of the Voigt profiles (of which the thermal profiles are a subset) until the residual signal is consistent with noise. This technique was motivated by the picture of the intergalactic medium as consisting of a smooth component which causes relatively little absorption and a set of clouds that satisfy the narrow-maximum-limit. For each cloud, the best-fit Voigt profile then yields its temperature and column density according to equation (6).

However, it is clear that for a general fluctuating medium, not all maxima in τ necessarily satisfy the conditions leading to equation (6). In fact, according to most structure formation theories, there invariably exist fluctuations in the intergalactic medium on scales larger than the thermal width. In the broad-maximum-limit, the shape of a local maximum in optical depth is determined by the distributions of n_{HI} and $|du/dx|$ around it. Each maximum in τ can still be identified as an absorption line and one can even apply standard techniques and try to fit its shape with superposition of the Voigt profiles. Given the best-fit Voigt profiles, one can assign a b -value (width of the profile) and a column density to each profile but it is no longer true, for instance, that the b -value thus obtained is equal to $\sqrt{2k_B T/m_p}$ (eq. [5]). A reasonable question to ask is whether there are other practical methods of identifying absorption lines and assigning column densities without assuming every absorption line consists of a superposition of the Voigt profiles. This will be discussed in Sec. 4.1. It should be borne in mind, however, that all existing observational data on the column density distribution are obtained using the Voigt-profile-fitting-technique, so for the purpose of comparing theory with these observations, it is important the line-identification algorithm one uses gives results consistent with the profile-fitting-technique.

In general, there are regions of high density and limited extent, galaxies for instance, which give rise to absorption profiles well approximated by the narrow-maximum-limit, but there are also regions in the intergalactic medium with gentle fluctuations where the broad-maximum-limit holds. Then there are those places where neither limit applies, in which cases, a full integration of equation (5) has to be carried out to compute the optical depth. To do so, one needs to know how the neutral hydrogen density, peculiar velocity and temperature vary with spatial position. This is the subject of the next section. In any case, the above discussion should make it clear that the quasar absorption spectrum contains a wealth of information on the intergalactic medium.

3. Ingredients for Generating Quasar Absorption Spectra

There are four quantities that go into the computation of the optical depth: temperature, peculiar velocity, overdensity and neutral fraction. That the temperature and peculiar velocity are important should be obvious from the expression for the absorption cross-section in equation (5). The temperature determines the extent of thermal broadening (b) and the peculiar velocity changes the frequency of the photon in the fluid rest-frame (eq. [3]). Let us define carefully what we mean by the other two quantities, the overdensity and the neutral fraction.

Suppose $n_{\text{H}}(\mathbf{x})$ is the total proper number density of all hydrogen species at position \mathbf{x} and \bar{n}_{H} is its spatial average. The overdensity δ_b , which describes the variation in space of $n_{\text{H}}(\mathbf{x})$, satisfies:

$$n_{\text{H}}(\mathbf{x}) = \bar{n}_{\text{H}} [1 + \delta_b(\mathbf{x})] , \quad \rho_b(\mathbf{x}) = \bar{\rho}_b [1 + \delta_b(\mathbf{x})] . \quad (8)$$

In the first expression, δ_b is defined as the number overdensity of hydrogen. In the second expression, we equate δ_b with the mass overdensity of baryons (ρ_b is the proper mass density of baryons and $\bar{\rho}_b$ is its mean), which is an excellent approximation for our application because there is no significant conversion of hydrogen into other elements, nor is there any interaction that could cause the spatial distribution of hydrogen to deviate significantly from that of other types of baryons.

What the Ly α absorption directly probes is not the total hydrogen density but its neutral component. The neutral fraction X_{HI} is defined by the following relation:

$$n_{\text{HI}}(\mathbf{x}) = n_{\text{H}}(\mathbf{x}) X_{\text{HI}}(\mathbf{x}) , \quad (9)$$

where n_{HI} is the proper number density of neutral hydrogen as a function of space. The neutral fraction is determined by the balance between recombination and ionization, the rates of which are dictated by the temperature and radiation intensity respectively.

In general, all four quantities, overdensity δ_b , peculiar velocity v_{pec} , temperature T and neutral fraction X_{HI} , are functions of position. In the next two sub-sections, we discuss first how to determine the spatial distributions of δ_b and v_{pec} , and second how T and X_{HI} vary with position through their dependence on δ_b . All quantities are evaluated at $\bar{z} = 3$. Although most of the material in this section is standard textbook fare, it consists of a somewhat unusual combination of methods, so it is worth going through the basic equations and stating our assumptions carefully.

3.1. The Zel'dovich Approximation

In cosmological models where dark matter (a term we use interchangeably with non-interacting matter) dominates the mass density of the universe, δ_b as defined in equation (8) coincides with the dark matter overdensity δ_{DM} on large scales. We define δ_{DM} in an analogous manner as before (eq. [8]):

$$\rho_{\text{DM}}(\mathbf{x}) = \bar{\rho}_{\text{DM}}[1 + \delta_{\text{DM}}(\mathbf{x})], \quad (10)$$

where ρ_{DM} is the mass density of dark matter at position \mathbf{x} and $\bar{\rho}_{\text{DM}}$ is its mean. The equality $\delta_b = \delta_{\text{DM}}$ is equivalent to the statement that the hydrogen density (which we assume is simply proportional to the baryon density) varies with position in the same manner as the dark matter density does. This is true on large scales where gas pressure is insignificant compared to the gravitational attraction of the dark matter, provided the baryons and dark matter start out having the same spatial distribution, which is approximately true for most popular cosmological models. Moreover, with no significant interaction that distinguishes between the two on large scales, the baryons and dark matter share the same peculiar velocity field. On small scales, however, gas pressure can cause the spatial distributions of baryons and dark matter and their velocities to differ. We will return to this point below.

Hence, on sufficiently large scales (how large is large, an obviously important question, will be addressed later), it is adequate to know the overdensity and peculiar velocity of the dark matter. The Zel'dovich approximation (Zel'dovich 1970) is a well-tested approximation to compute the density and velocity distributions of dark matter in the mildly nonlinear regime ($\delta_{\text{DM}} \lesssim 5$) before orbit-crossing. The reader is referred to the article by Shandarin and Zel'dovich (1989) for a comprehensive review (see also Hui and Bertschinger 1996 for an alternative formulation of the approximation).

The starting point of the Zel'dovich approximation is the following equation for the displacement of a given mass element or particle:

$$\mathbf{x}(\mathbf{q}, t) = \mathbf{q} + D_+(t) \nabla_{\mathbf{q}} \psi(\mathbf{q}), \quad (11)$$

The coordinate \mathbf{q} is the initial position of the mass element and \mathbf{x} is its comoving position as a function of time. The displacement is then $D_+(t) \nabla_{\mathbf{q}} \psi(\mathbf{q})$. Its time dependent part $D_+(t)$ is the linear growth factor (Peebles 1980), which, for a universe with critical matter density, can be equated with a , the Hubble scale factor. The time independent function $\nabla_{\mathbf{q}} \psi(\mathbf{q})$ is determined by initial conditions. Growing mode initial conditions dictate that it is curl-free, hence its form as the gradient of the potential ψ ($\nabla_{\mathbf{q}}$ is the spatial gradient in q space).

Expressions for the peculiar velocity and overdensity follow immediately from equation (11):

$$\mathbf{v}_{\text{pec}} = a\dot{D}_+ \nabla_{\mathbf{q}} \psi, \quad 1 + \delta_{\text{DM}} = \det^{-1} \left[\delta_{ij} + D_+(t) \frac{\partial^2 \psi}{\partial q_i \partial q_j} \right]. \quad (12)$$

The dot in the first expression denotes differentiation with respect to proper time t . The peculiar velocity is defined by $\mathbf{v}_{\text{pec}} = a\mathbf{dx}/dt$. The second expression follows from mass conservation i.e. $(1 + \delta_{\text{DM}})d^3x = d^3q$. The right hand side of the second expression is simply the Jacobian of the q - x transformation matrix.

The function $\psi(\mathbf{q})$ contains all the information on the specific cosmological model one chooses to study. For the cosmological models we study in this paper, it is a Gaussian random field in \mathbf{q} space. Suppose $\tilde{\psi}(\mathbf{k})$ is its Fourier counterpart defined by $\psi = \int d^3k \tilde{\psi} e^{i\mathbf{k}\cdot\mathbf{q}}$. The two-point correlation of $\tilde{\psi}$ is related to the commonly used power spectrum P by

$$\langle \tilde{\psi}(\mathbf{k}) \tilde{\psi}^*(\mathbf{k}') \rangle = k^{-4} P(k) \delta^3(\mathbf{k} - \mathbf{k}'), \quad (13)$$

where P is related to the root-mean-squared (rms) linear overdensity fluctuation by

$$\langle \delta^2 \rangle = D_+^2(t) \int_0^\infty 4\pi P(k) k^2 dk. \quad (14)$$

Note that $D_+^2 = (1 + \bar{z})^{-2}$ for a universe with critical matter density, choosing $D_+ = 1$ today.

To produce a realization of the density and velocity fields for a given cosmological model, we employ the following procedure: first, we use the corresponding power spectrum to generate the Gaussian random field $\psi(\mathbf{q})$ on a grid; second, we displace particles from their initial grid positions (\mathbf{q}) according to equation (11) for $D_+(t)$ corresponding to $\bar{z} = 3$; third, a peculiar velocity is assigned to each particle according to the first expression in equation (12); finally, we use the TSC (Triangular-Shaped density Cloud) scheme (Hockney & Eastwood 1988) to interpolate the particle positions and velocities to become momentum and mass densities on the grid and divide one by the other to obtain the velocity itself. The interpolation to obtain mass density is our way of enforcing mass conservation, as is expressed in the second expression of equation (12). In the last procedure, we smooth the momentum and mass density fields over a small number of grid cells (in fact, we use one and have checked that the precise number is not important as long as it is small) before performing the division to obtain the velocity field so that we have well-defined velocities even in places with zero density after the TSC interpolation (Kofman et al. 1994). Any line of sight can then be chosen through the simulation box and the above set of steps gives the overdensity and peculiar velocity (in fact only the component parallel to the line of sight is needed) at each grid point on it.

The procedure just outlined is very efficient because there is no need to integrate any equation of motion. One simply multiplies the displacement of each particle by an appropriate factor of $D_+(t)$. However, the first step of the procedure has to be slightly modified to address two problems.

The first one is orbit-crossing. The Zel'dovich approximation is known to predict too rapid growth of the thickness of the post-collapse pancake (Shandarin and Zel'dovich 1989). A number of cures have been proposed (Kofman, Pogosyan, & Shandarin 1990; Matarrese et al. 1992; Brainerd, Scherrer, & Villumsen 1993; Bagla & Padmanabhan 1994) but the one that consistently gives good agreement with N-body simulations is the truncated Zel'dovich approximation (Kofman 1991; Coles, Melott & Shandarin 1993; Melott, Buchert & Weiß 1995). The basic idea is to smooth the initial power spectrum on small scales so that the amount of orbit-crossing that might have occurred by the time of interest is not significant enough to destroy the accuracy of the Zel'dovich approximation on large scales, where the fluctuations are still mildly nonlinear. The initial power spectrum $P(k)$ is multiplied by a Gaussian smoothing kernel of the form e^{-k^2/k_S^2} , before it is used to generate the Zel'dovich displacement field (eq. [13]). (This is equivalent to smoothing the initial density field $\delta(\mathbf{x})$ through the following convolution: $(2\pi k_S^{-2})^{-0.5} \int \delta(\mathbf{x}') e^{-(k_S^2|\mathbf{x}-\mathbf{x}'|^2/2)} d^3x'$.) The smoothing wavenumber k_S is chosen according to the following prescription

$$k_S = 1.5 k_{\text{NL}}, \quad \text{where } 1 = D_+^2(t) \int_0^{k_{\text{NL}}} 4\pi P(k) k^2 dk. \quad (15)$$

Note that $P(k)$ above is the initial power spectrum before any smoothing. The proportionality constant between k_S and k_{NL} actually depends somewhat on the power spectrum, with more smoothing (smaller k_S) required for models that have relatively more power on small scales (Melott 1994). The choice above has been shown to give good agreement with N-body simulations for CDM models (Melott et al. 1995). We will see that for those CHDM models with relatively little power on small scales, the precise value of k_S is not important. The procedure described above is commonly called the truncated Zel'dovich approximation.

The second problem is one we have pointed out before, namely that δ_{DM} is not necessarily equal to δ_b (which is what we are interested in ultimately) on small scales. In linear theory, it is possible to show that for a dark matter dominated universe, the Fourier components of the two quantities obey $\tilde{\delta}_b(k) = \tilde{\delta}_{\text{DM}}(k)$ when $k \ll k_J$ and $\tilde{\delta}_b(k) = k_J^2 \tilde{\delta}_{\text{DM}}(k)/k^2$ when $k \gg k_J$. Under some restrictive assumptions (see Appendix A), it can be shown that $\tilde{\delta}_b(k) = \tilde{\delta}_{\text{DM}}(k)(1 + k^2/k_J^2)^{-1}$. The quantity k_J^{-1} is known as the Jeans scale and is defined by:

$$k_J^{-1} = \sqrt{\frac{\gamma k_B \bar{T}}{4\pi a^2 G \mu \bar{\rho}_{\text{DM}}}}, \quad (16)$$

where k_B is the Boltzmann constant, \bar{T} is the spatially averaged temperature of the gas, μ is the mean mass per particle (for fully ionized gas with primordial abundances, it is about $0.6m_p$ where m_p is the mass of the proton) and γ describes the relation between the temperature T (the actual, not average, value) and $1 + \delta_b$: $T \propto (1 + \delta_b)^{\gamma-1}$. Note that γ does not necessarily equal $5/3$ unless the gas behaves adiabatically. The proofs of the above assertions can be found in the Appendix A (see also Bi et al. 1992; Peebles 1993). It is sufficient to note here that in the linear regime, the baryon density field is smoother than that of the dark matter on small scales due to the effect of gas pressure.

Now, the above relations between $\tilde{\delta}_b$ and $\tilde{\delta}_{\text{DM}}$ hold only in the linear regime when both quantities are small. To take into account the effect of gas pressure in the mildly nonlinear regime, one possibility is to smooth the initial power spectrum by a factor of $(1 + k^2/k_J^2)^{-2}$ before generating the displacement field, similar to what is done in the case of the truncated Zel'dovich approximation. This method was used by Reisenegger & Miralda-Escudé (1995) to study the fluctuating Gunn-Peterson effect. In practice, we smooth the initial power spectrum by a Gaussian kernel e^{-k^2/k_J^2} and find that the two ways of smoothing give very similar column density distributions.

To give an idea of scale, for $\gamma = 1.5$, $\bar{T} = 10^4$ K and a universe at critical density, k_J is equal to $16.8 h \text{ Mpc}^{-1}$. It turns out that for all models considered in this paper except the $\Omega_\nu = 0.2$ CHDM models, the truncation scales k_S^{-1} according to equation (15) are larger than k_J^{-1} (eq. [16]), for reasonable ranges of temperature and γ . For these models, it is unnecessary to smooth the initial power spectrum over the Jeans scale because the truncated Zel'dovich approximation already prescribes more smoothing. The opposite is true for the $\Omega_\nu = 0.2$ CHDM models. In fact, the amount of small scale power is so insignificant for these models that the precise scale of smoothing does not affect the column density distribution for column densities of interest (Sec. 8). Orbit-crossing is probably not very severe for this class of models. Hence, uncertainty in the Jeans smoothing scale due to uncertainties in the temperature and equation of state of the intergalactic medium is not a concern.

To sum up, we smooth the initial power spectrum on the scale of k_S^{-1} (eq. [15]) or k_J^{-1} (eq. [16]), depending on which is bigger, before it is used to generate the displacement field (eq. [13]) (except for a few test-cases discussed in Sec. 7). The rest of the procedure to obtain the overdensity δ_b and peculiar velocity v_{pec} on a grid follows as before. The implicit assumption underlying the whole procedure is that fluctuations on scales smaller than the smoothing scale do not contribute significantly to the number of absorption lines at our column densities of interest, about $10^{12.5} - 10^{14.5} \text{ cm}^{-2}$. The upper limit is related to the maximum overdensity (δ_b around 5) beyond which the Zel'dovich approximation

is not expected to be reliable and the lower limit is set by our resolution (see Sec. 5 for more details). Note that while the Jeans scale smoothing is meant to capture the actual smoothing of the density field by gas pressure, the nonlinear scale smoothing is an approximation technique to avoid the problem of orbit-crossing. As such, the validity of the latter in the present application has to be checked. We show in Sec. 5 a comparison between the column density distribution computed using the approximate method described here and that using a full hydrodynamic simulation. The level of agreement lends support to our assumption. Another consistency check is to see if shock-heating is important for regions with overdensities (or underdensities) associated with the above range of column densities. A plot of density versus temperature like Fig. 2 in Weinberg et al. (1996) shows that shock-heating, and by extension orbit-crossing, is not important for regions of underdensity or low overdensity.

3.2. The Thermal and Ionization State

Given the evolution of δ_b predicted by the Zel'dovich approximation, it is possible to integrate evolution equations for T and for X_{HI} as well as the abundance of other species to obtain their relations with δ_b .⁸

Details of the computation will be given in a separate paper (Hui and Gnedin 1996). A brief discussion can be found in Appendix B of this paper. We summarize the main relevant conclusions here.

First, ionization equilibrium is maintained at high accuracy except during the period of initial reionization. Ionization equilibrium implies that the neutral hydrogen fraction (eq. [9]) satisfies

$$X_{\text{HI}} \sim 1.6 \times 10^{-6} \left(\frac{T}{10^4 K} \right)^{-0.7} \left(\frac{\Omega_b h^2}{0.0125} \right) \left(\frac{J_{\text{HI}}}{0.5} \right)^{-1} (1 + \delta_b) \left(\frac{1 + \bar{z}}{4} \right)^3, \quad (17)$$

where we have adopted the approximate form of the recombination coefficient of hydrogen: $4.29 \times 10^{-13} (T/10^4 \text{K})^{-0.7} \text{cm}^3 \text{s}^{-1}$, which is sufficient for our purpose (see Hui & Gnedin 1996 for a more accurate analytical fit). The quantity J_{HI} is a measure of the radiation intensity

⁸Since these equations are local, in the sense that each mass element evolves independently of the others, there is actually no need to generate a full three-dimensional realization for the purpose of studying the thermal and ionization evolution. A simpler approach is to generate a set of eigenvalues of the deformation matrix $\partial^2 \psi / \partial q_i \partial q_j$ according to the prescription of Doroshkevich (1970) and determine the density evolution through the second part of equation (12).

defined as follows (analogous to the definition in Miralda-Escudé et al. 1996 but differs by a factor of 10^{-21} ergs Hz $^{-1}$ s $^{-1}$ cm $^{-2}$ ster $^{-1}$):

$$J_{\text{HI}} = \frac{\int_{\nu_{\text{HI}}}^{\infty} 4\pi J_{\nu} \sigma_{\text{HI}} \frac{d\nu}{h\nu}}{\int_{\nu_{\text{HI}}}^{\infty} 4\pi \sigma_{\text{HI}} \frac{d\nu}{h\nu}} (10^{-21} \text{ ergs Hz}^{-1} \text{ s}^{-1} \text{ cm}^{-2} \text{ ster}^{-1})^{-1}, \quad (18)$$

where J_{ν} is the specific intensity as a function of frequency ν in the units given above, h is the Planck constant, $h\nu_{\text{HI}}$ is 13.6 eV and σ_{HI} is the ionization cross-section. The photoionization rate is simply equal to $4 \times 10^{-12} J_{\text{HI}} \text{ s}^{-1}$.

Observations indicate that J_{HI} is between about 0.1 and 2.0 for $\bar{z} = 2 - 4$ (Batjlik, Duncan & Ostriker 1988; Lu et al. 1991; Bechtold 1994; Giallongo et al. 1996; Cooke, Espey & Carswell 1997). A perhaps more common way of characterizing the radiation intensity is to quote its value, often referred to as J_{912} , at $\nu = \nu_{\text{HI}}$ or at wavelength 912 Å, in units of ergs Hz $^{-1}$ s $^{-1}$ cm $^{-2}$ ster $^{-1}$. The relation between J_{912} and J_{HI} depends on the spectrum. A good approximation for reasonable slopes of the spectrum right above ν_{HI} ($J_{\nu} \propto \nu^{-m}$ for m between 1 and 1.5) is $J_{\text{HI}} = 0.7 J_{912} / 10^{-21}$.

Second, we find that

$$T = T_0 (1 + \delta_b)^{\gamma-1}, \quad (19)$$

where T_0 is not dependent on position, is a good approximation for overdensities of interest, $\delta_b \lesssim 5$, with a little flattening at the low end (δ_b close to 0.1) for some reionization scenarios. We will call this our equation of state. Note that this implies that the spatial dependence of T (and by extension X_{HI}) is completely determined by that of δ_b , which is true for unshocked gas. Similar power law relations between the overdensity and the temperature can be seen in Fig. 2 of Weinberg et al. (1996) for low overdensity.

Third, both T_0 and γ depend on the reionization history, the reasonable ranges being $1.2 < \gamma < 1.7$ and $3000 K < T_0 < 30000 K$ at $\bar{z} = 3$. It is shown in Hui & Gnedin (1996) that $1.3 < \gamma < 1.62$ at $\bar{z} = 3$ if the universe reionizes before $\bar{z} = 5$, assuming uniform radiation field. We allow for a larger range here.

Combining equations (19) and (17), it can be seen that the neutral hydrogen fraction is proportional to $(1 + \delta_b)^{1-0.7(\gamma-1)}$.

In conclusion to Sec. 3, we have outlined a procedure to use the Zel'dovich approximation, with appropriate initial smoothing, to produce a realization of δ_b and v_{pec} as a function of position, and we have also shown how the relations between T , X_{HI} and δ_b can be obtained (eq. [19] and [17]). All of them enter into the calculation of the optical depth τ (eq. [1] or [5]). We can compute $e^{-\tau}$, called the transmission, which is the ratio of the observed to the emitted intensities. Observationally, its measurement requires knowledge of

the quasar emission spectrum. Moreover, one must carefully choose the range of frequencies to consider if one is to limit the source of absorption to that due to the Ly α transition. For a discussion of these issues, the reader is referred to Press, Rybicki and Schneider (1993). To produce a realistic spectrum, one should also add noise and convolve the transmission with a window function to mimic instrumental resolution. This is important for a detailed comparison between theories and observations, which we will defer to latter work. Our x space grid cells, depending on the particular simulation, have sizes ranging from 0.028 Mpc to 0.075 Mpc comoving. Note that the true resolution in velocity space is not uniform because peculiar velocity varies from one place to another. Without peculiar velocity, the above grid cell sizes correspond to velocity cells of $2.8 - 7.5 \text{ km s}^{-1}$, for $h = 0.5$ at $\bar{z} = 3$ (eq. [3]). The true velocity resolution is probably a little worse than that. As a comparison, high quality Keck Telescope data have a Full-Width-Half-Maximum of about 7 km s^{-1} and signal to noise per pixel of the order of 30 or higher (Hu et al. 1995; Lu et al. 1996).

4. The Peculiar Velocity: its Effects on Line Shapes and the Column Density Distribution

We show in this section that while the peculiar velocity plays an important role in determining the absorption profiles, its effect on the column density distribution is minor. The procedures to obtain the column density distribution are discussed first.

4.1. Line Identification and the Column Density Distribution

Fig. 1 and Fig. 2 show the velocity, density and transmission ($e^{-\tau}$) along two lines of sight for a $\sigma_8 = 0.7$ CDM simulation, with $h = 0.5$ (see Table 1). The significance of the dashed transmission profile will be explained in the next sub-section. The thermal and ionization parameters are described in the caption of Fig. 1. The truncation scale k_S (eq. [15]) is 2.3 Mpc^{-1} . The transfer function is taken from Ma (1996). We find that using instead the transfer function of Bardeen et al. (1986) makes almost no difference to the resulting column density distribution, for the range of column densities considered.

The first thing to note is that for the given parameters,

$$b \equiv \sqrt{\frac{2k_B T_0}{m_p}} = 13 \text{ km s}^{-1} (1 + \delta_b)^{1/4}. \quad (20)$$

This might seem to be too small because the observed lower limit of the b -value is about $15 - 20 \text{ km s}^{-1}$ (Hu et al. 1995; Lu et al. 1996). There are two points to be made. First,

T_0 is the temperature of the gas at $\delta_b = 0$. The observed b -values might originate from regions at higher δ_b . It is true though that the $1/4$ power of $1 + \delta_b$ does not help very much. Second, a distinction should be made between the observed b -value and the b defined above. The observed b -value is obtained by fitting the quasar spectrum with superpositions of the Voigt profiles. Each Voigt profile yields a column density and a b -value. All the density peaks that give rise to absorption troughs in Fig. 1 and Fig. 2 have velocity widths larger than or comparable to the small thermal width defined in equation (20). Therefore the narrow-maximum-limit (eq. [6]) does not apply and the absorption troughs do not exactly have the Voigt profile shapes. The b -value obtained from the best-fit Voigt profile of a given absorption trough does not necessarily correspond to the thermal width in equation (20). It should also be emphasized that the recent hydrodynamic simulations of the Ly α forest, which have been so successful in accounting for a lot of its observed properties, have similarly low temperatures (see for instance Weinberg et al. 1996 ⁹).

One might wonder if there exists an alternative spectrum reduction method where the Voigt profile is not assumed to be the fundamental shape of absorption troughs, and for such a method, how the column density is assigned to each trough. The Voigt-profile-fitting-technique is nonetheless very important because it is how all existing observational data on the column density distribution are obtained.

An alternative line identification algorithm was proposed by Miralda-Escudé et al. (1996) and was also used by Hernquist et al. (1995). First a transmission ($e^{-\tau}$) threshold is chosen. Any part of the spectrum that is continuously below the threshold is identified as an absorption line. The column density associated with it is defined by

$$N_{\text{HI}} \equiv \frac{1}{\sigma_{\alpha 0}} \int_{\text{line}} \tau(u_{\circ}) \frac{du_{\circ}}{c}, \quad (21)$$

where $\sigma_{\alpha 0}$ is defined after equation (5). The limits of integration are taken to be over the absorption line, i.e. where the transmission is continuously below the threshold. Note that if the narrow-maximum-limit or the thin cloud assumption were to hold, equation (6) can be substituted into equation (21) to show that N_{HI} does correspond to $\int n_{\text{HI}} dx / (1 + z)$, assuming the threshold is high enough so that most of the Voigt profile is included in the definition of the absorption line.

Let us call the above procedure the Threshold-Algorithm. We show in Fig. 3 the

⁹Their output is at redshift of 2 and so naturally they have a lower temperature. In general, the temperature T_0 is dependent on the reionization history of the universe: crudely speaking, the closer the epoch of reionization is to the epoch of observation ($\bar{z} = 3$ in our case), the higher the temperature. Assuming reionization occurs before a redshift of 5, say, puts an upper bound on T_0 (Hui and Gnedin 1996).

column density distribution computed according to the algorithm (Crosses). The symbol $d^2 N_{\text{Ly}\alpha} / dN_{\text{HI}} / dz$ denotes the number of absorption lines per unit column density per unit redshift. The reason for the chosen range of column densities will be given in Sec. 5. The transmission is chosen to be at the mean transmission of 0.89.

The Threshold-Algorithm has the tendency to underestimate the number of absorption lines compared to the Voigt-profile-fitting-technique. One reason is that it does not deblend. In other words, a given absorption line according to the Threshold-Algorithm may contain more than one minimum in transmission. Such an absorption line would be broken up to a few lines if the Voigt-profile-fitting-technique is employed. To demonstrate this effect, we modify the Threshold-Algorithm: for each (parent) absorption line identified, we break it up into individual components (children) where each component is bordered by local maxima in the transmission within the confines of the parent. The column density for each child component is defined similarly as in equation (21) and the limits of integration are taken to be the boundaries of each component. We will call it the Threshold-Deblending-Algorithm.

The resulting column density distribution is denoted by the square symbols in Fig. 3 for the transmission threshold of 0.89. One can see that indeed the number of lines of low column densities go up. We should emphasize however that the Threshold-Deblending-Algorithm cannot be used to analyze observational data without modifications because in real life, noise creates local transmission maxima within any parent absorption line.¹⁰

For now, the Threshold-Algorithm is adopted as a simple way to identify lines and assign column densities, which we will use to study the effects of the peculiar velocity on the column density distribution.

4.2. The Role of Peculiar Velocities

The following experiment is performed to investigate the importance of peculiar velocities. We generate absorption spectra and compute the column density distribution using the same density field as that used to produce the solid curves in Fig. 1, Fig. 2 and the crosses in Fig. 3 but we set all peculiar velocities to zero.

Let us first examine some examples of the absorption spectra. The dashed curves in Fig. 1 and Fig. 2 are the resulting spectra after putting all peculiar velocities to zero.

¹⁰In fact, numerical noise can also have the same effect. We check it by defining local maxima in two ways: local maxima over three cells and local maxima over five cells with the slope on either side of the maxima not changing signs. It turns out the resulting column density distributions are almost the same.

A comparison of the dashed absorption spectrum with its solid counterpart in each figure shows that the peculiar velocities play an important role in determining the shapes of absorption lines. Without peculiar velocities, the shapes of absorption troughs mirror closely (perhaps a little thermally-broadened compared to) those of the density peaks while with nonzero peculiar velocities, the absorption troughs can have quite different shapes from the underlying density field. Peculiar velocities can add or erase structures. An example of the former can be found in the pair of density peaks around $x = 9$ Mpc and their corresponding absorption profiles in Fig. 1. An example of the latter can be found in the density peak(s) around $x = 7$ Mpc and the corresponding absorption trough(s) in Fig. 2.

Broadly speaking, the effects of peculiar velocities on absorption spectra fall into three categories. They are distinguished by the value of du/dx (u is defined in eq. [3]). First, there are regions in space where the peculiar velocity gradient is small so that du/dx is almost equal to its Hubble value $\bar{H}/(1 + \bar{z})$ (eq. [3]). An example is the density peak around $x = 2.2$ Mpc in Fig. 2. The peculiar velocity shifts the position of the associated absorption trough but does not affect its shape.

Second, there are places where the peculiar velocity gradient is opposite in sign and comparable in magnitude to $\bar{H}/(1 + \bar{z})$, in which case $|du/dx|$ becomes very small. Suppose also that $|d^2u/dx^2|$ is small. The implication is that a small range in u corresponds to a relatively large range in x . See for instance the density peak(s) around $x = 7$ Mpc in Fig. 2, which is a really broad structure in x space but is relatively narrow in u space if peculiar velocities are not put to zero. The small $|du/dx|$ or the converging peculiar velocity flow around it helps to produce a narrow absorption trough (second panel from the top in Fig. 2). Contrast it with the corresponding absorption feature in the top panel of the same figure, where peculiar velocities are set to zero. The limiting case where $|du/dx|$ exactly vanishes is called a velocity caustic (McGill 1990).

Third, there are regions where the peculiar velocity gradient dominates in such a way that du/dx is negative and $|du/dx|$ is not small. An example can be found around the pair of density peaks at $x = 9$ Mpc in Fig. 1. This is where multiple-streaming occurs. A given range in u corresponds to disjoint pieces in x space. As a result, the shapes of the associated absorption troughs are significantly different from those of the underlying density peaks.

The three categories can be shown to correspond to the three evolutionary stages of a pancake collapsing along the line of sight (McGill 1990). Restricting equations (11) and (12) to one dimension and putting it into equation (3), one obtains:

$$\frac{du}{dx} = \dot{a} \left(1 + 2a \frac{d^2\psi}{dq^2} \right) \left(1 + a \frac{d^2\psi}{dq^2} \right)^{-1}, \quad (22)$$

where we have assumed a universe of critical matter density so that $D_+ = a$. Restricting equation (12) to one dimension, it can also be shown that

$$1 + \delta_b = \left(1 + a \frac{d^2\psi}{dq^2} \right)^{-1}, \quad (23)$$

where we have replaced δ_{DM} by δ_b assuming the appropriate initial smoothing has been carried out as indicated in Sec. 3.1. As a grows, it can be seen that du/dx goes through the three different regimes outlined above for negative $d^2\psi/dq^2$. At the velocity caustic where $du/dx = 0$, it can be shown that $\delta_b = 1$ (McGill 1990). This conclusion does not hold in general of course because pancakes can collapse in directions different from the line of sight. But it is true that velocity caustics are often found in regions of slight overdensities.

In principle, at a velocity caustic, an absorption line can arise even without any variation in the density field at all (eq. [5]). In practice, one expects that converging peculiar velocity flows are accompanied by density peaks. This is consistent with the few examples we have seen.

Next, we consider how the column density distribution changes when the same density field is used but all the peculiar velocities are put to zero. This is shown in Fig. 3.

The mean transmission of the spectra computed with zero peculiar velocities differs from the mean transmission of the full spectra by less than a percent. It is used as the transmission threshold in the line identification procedure for both analyzes. The resulting column density distributions are very similar.

Hence, the peculiar velocity plays a relatively minor role in determining the column density distribution. It changes the shapes of absorption troughs without altering the overall number of lines and their column densities. This serves to motivate an approximation we will introduce in the next section.

A final note on velocity caustics. The reader might worry that at a velocity caustic, the optical depth may diverge while it is clear from equation (1) that for a finite number density of neutral hydrogen, the optical depth should always be a finite quantity. The resolution is that close to a velocity caustic at $u = u_c$, du/dx goes like $|u - u_c|^{1/2}$ (provided the second derivative of u with respect to x is nonzero, otherwise it will be $(u - u_c)^{2/3}$ if the third derivative does not vanish and so on, by simple Taylor series expansion; see Shandarin and Zel'dovich 1989 for a similar analysis applied to real caustics as opposed to velocity caustics; orbit-crossing occurs in the former but not the latter). So under the integration in equation (5), the optical depth remains finite. We note also that because of the singular nature of $(du/dx)^{-1}$ around $u = u_c$, the derivation leading to equation (7) breaks down at a velocity caustic.

5. The Statistics of Density Peaks

In this section we explore a simple approximation in which each density peak in x space is identified with an absorption line. This is motivated by the fact that peculiar velocities do not play a major role in determining the column density distribution and that each maximum in density corresponds to a minimum in transmission or maximum in absorption if the peculiar velocities are set to zero and if the maximum in density is separated from other maxima by a distance larger than that given by the thermal broadening width.

To calculate $d^2N_{\text{Ly}\alpha}/dN_{\text{HI}}/dz$, we relate dz and dx by ignoring peculiar velocities: $dz = c^{-1}\bar{H}dx$. Hence

$$\frac{d^2N_{\text{Ly}\alpha}}{dN_{\text{HI}}dz} = \frac{d^2N_{\text{pk}}}{dN_{\text{HI}}dx} \frac{c}{\bar{H}}, \quad (24)$$

where $dN_{\text{pk}}/dN_{\text{HI}}/dx$ is the average comoving number density of density peaks along a random line of sight per unit column density, \bar{H} is the Hubble constant at the redshift of interest.

For each density peak, we need a simple prescription for assigning a column density. To that end, we perform the following expansion around each density maximum:

$$\ln[n_{\text{HI}}(x)] = \ln[n_{\text{HI}}(x_{\text{pk}})] + \frac{1}{2} \left. \frac{d^2 \ln[n_{\text{HI}}]}{dx^2} \right|_{x=x_{\text{pk}}} (x - x_{\text{pk}})^2. \quad (25)$$

It is a straightforward Taylor expansion around the position of the peak x_{pk} . The second derivative in the last term is negative. The rationale behind expanding $\ln[n_{\text{HI}}]$ rather than n_{HI} itself is that n_{HI} is supposed to fall off quickly far away from the peak (until, of course, another peak is encountered). In other words, the above expansion implies that n_{HI} has a Gaussian fall-off (instead of a power-law one if n_{HI} itself were Taylor expanded). In a sense, this is close in spirit to the Voigt-profile-fitting-technique. Suppose the broad-maximum-limit (eq. [7]) holds so that the local optical depth is simply proportional to the number density of neutral hydrogen if one ignores peculiar velocities. Then, fitting a minimum in optical depth with the Voigt or thermal profile (eq. [5]) is equivalent to fitting the corresponding neutral hydrogen density peak with a Gaussian.

We then assign the following column density to the density peak:

$$N_{\text{HI}} = \int_{\text{pk}} \frac{dx}{1 + \bar{z}} n_{\text{HI}}(x) = n_{\text{HI}}(x_{\text{pk}})(1 + \bar{z})^{-1} \sqrt{2\pi} \left. \left(\frac{-d^2 \ln[n_{\text{HI}}]}{dx^2} \right)^{-1} \right|_{x=x_{\text{pk}}} \quad (26)$$

where equation (25) has been used and where \int_{pk} denotes integration around the peak until it decays sufficiently. All x dependent terms on the right hand side are evaluated at

$x = x_{\text{pk}}$. The above equation is also derived by the authors in a separate paper, using the Stationary Phase Method (Gnedin and Hui 1996).

Using equations (17) and (19), the above can be rewritten as:

$$N_{\text{HI}} = 1.63 \times 10^{13} \text{ cm}^{-2} \left(\frac{T_0}{10^4 K} \right)^{-0.7} \left(\frac{\Omega_b h^2}{0.0125} \right)^2 \left(\frac{J_{\text{HI}}}{0.5} \right)^{-1} \left(\frac{1 + \bar{z}}{4} \right)^5 \left(\frac{2 - 0.7(\gamma - 1)}{1.65} \right)^{-0.5} A \quad (27)$$

where A is defined by

$$A \equiv (1 + \delta_b)^{2-0.7(\gamma-1)} \left(\frac{-d^2 \ln[1 + \delta_b]}{dx^2} \right)^{-\frac{1}{2}} \Big|_{x=x_{\text{pk}}}, \quad (28)$$

with x being measured in Mpc.

We will refer to our method as the Density-Peak-Ansatz. It consists of two parts: 1. associate each density peak in x space with an absorption line; 2. assign a column density to each density peak according to equation (27).¹¹

Making use of equations (24) and (27), the column density distribution can be written as

$$\frac{d^2 N_{\text{Ly}\alpha}}{dN_{\text{HI}} dz} = 6.25 \times 10^{-14} \text{ cm}^2 \left(\frac{T_0}{10^4 K} \right)^{0.7} \left(\frac{\Omega_b h^2}{0.0125} \right)^{-2} \left(\frac{J_{\text{HI}}}{0.5} \right) \left(\frac{1 + \bar{z}}{4} \right)^{-5} \left[\frac{2 - 0.7(\gamma - 1)}{1.65} \right]^{0.5} \frac{c}{\bar{H}} \frac{d^2 N_{\text{pk}}}{dA dx}, \quad (29)$$

where x and $c\bar{H}^{-1}$ are in the same unit of Mpc. Most of the factors above come from the scaling between A and N_{HI} , and c/\bar{H} provides the conversion from comoving coordinate x to redshift z . The last factor $d^2 N_{\text{pk}}/dA/dx$ involves is the number density of peaks in x space having the quantity A within the range dA .

Let us define $\xi \equiv \ln[1 + \delta_b]$. Suppose one is given $P(\xi, \xi', \xi'') d\xi d\xi' d\xi''$ which is the probability that ξ and its first and second derivatives with respect to x fall in the specified ranges at a point. Then,

$$\frac{dN_{\text{pk}}}{dx} = \int_{-\infty}^{\infty} d\xi \int_{-\infty}^0 d\xi'' |\xi''| P(\xi, \xi' = 0, \xi''), \quad (30)$$

¹¹Strictly speaking, care should be taken not to count peaks that are separated in velocity space by distance much less than the thermal width as contributing to more than one absorption line. We will address this later in the section.

where $\frac{dN_{\text{pk}}}{dx}$ is the integral of $\frac{d^2N_{\text{pk}}}{dAdx}$ over all A (Bardeen et al. 1986).

By a change of variable and a differentiation and making use of equation (28), one can obtain

$$\frac{d^2N_{\text{pk}}}{dAdx} = \frac{1}{[2 - 0.7(\gamma - 1)]A} \int_{-\infty}^0 d\xi'' |\xi''| P(\xi, \xi' = 0, \xi'') \quad (31)$$

where ξ should be expressed in terms of ξ'' and A using equation (28).

Note that the above two equations are completely general and no assumption about the Gaussianity of the underlying fields has been made. The hard part is of course to come up with the probability function P . The one point probability distribution of just ξ or density has been calculated for the Zel'dovich approximation (Kofman et al. 1994). We find the one point joint-probability distribution of density and its first and second derivatives along a line of sight difficult to calculate analytically for the Zel'dovich approximation. A numerical approach is adopted in this paper and the number of peaks is counted along random lines of sight in actual three-dimensional realizations. In a separate paper, we discuss an analytical calculation based upon not the Zel'dovich approximation but the lognormal approximation, where ξ is assumed to be a Gaussian random field (Gnedin and Hui 1996). A comparison between the two will be made here.

5.1. Testing the Density-Peak-Ansatz

We test the Density-Peak-Ansatz in two different ways. First, we make a scatter plot of the column density obtained using the Threshold-Deblending-Algorithm versus the column density obtained by searching for the maximum density peak that contributes to each absorption line identified using the threshold method and then applying equation (27). The result is shown in Fig. 4. It shows that while the agreement is far from perfect, the column densities assigned using the Density-Peak-Ansatz and using the Threshold-Algorithm are broadly consistent.

The important question, however, is whether the Density-Peak-Ansatz, coupled with the Zel'dovich approximation with appropriate initial smoothing, gives the correct number of absorption lines as a function of column density. We compare the column density distribution obtained using our approximate methods against that obtained by applying the Voigt-profile-fitting-technique to synthetic spectra from a full hydrodynamic simulation (see discussion below and Zhang et al. 1996 for details). This is done in Fig. 5. Note that the values of γ and T_0 given in the caption of Fig. 5 is obtained directly from the hydrodynamic simulation. The temperature-density relation is not an exact power law but is well approximated by one for the relevant range of densities. We also put in the same

figure the column density distribution obtained using the Threshold-Algorithm, coupled with the Zel'dovich approximation. The predictions of the lognormal approximation are shown as well for comparison.

The level of agreement between the exact hydrodynamic computation and our calculation based on the Density-Peak-Ansatz coupled with the Zel'dovich approximation is encouraging. Two sets of points are shown for our approximate calculation using the Density-Peak-Ansatz, one (open triangles) with exactly the same box size and grid spacing as the hydrodynamic simulation and the other (open squares) with larger box size and smaller grid spacing. They both agree very well with the exact computation. We will explore the effects of changing the resolution in the next sub-section. A third set of points (crosses) shows that the Threshold-Algorithm described in Sec. 4.2 underestimates the number of lines at low column densities.

The agreement between the results of the hydrodynamic simulation and our approximation method is perhaps telling us something interesting about the low column density systems. Note that for the Zel'dovich approximation computations presented in Fig. 5, an initial smoothing scale ($k_S = 2.3 \text{ Mpc}^{-1}$) larger than the Jeans length ($k_J = 8.4 \text{ Mpc}^{-1}$) was chosen to deal with the problem of orbit-crossing. The agreement can then be understood as a result of relatively little contribution to the low column density systems ($10^{12.5} - 10^{14.5} \text{ cm}^{-2}$) from structure on small length scales suppressed by our k_S^{-1} smoothing even though those scales could be larger than the Jeans length. The low column density systems mostly consist of relatively broad density peaks.

Some explanation is also in order regarding the spectral analysis method used by Zhang et al. (1996) in obtaining the distribution shown in Fig. 5. It consists of identifying absorption features above a specified opacity and deblending them into individual lines centered at local maxima in optical depth and fitting each with a suitable Voigt profile. This procedure is designed to be similar to most observers' analysis techniques but is not exactly the same. In particular most observers' method consists of seeking a "minimal" set of Voigt profiles, the superposition of which reproduces the input absorption spectrum to within some specified error consistent with noise. It should be noted, however, that the definition of "minimal" tends to vary from one observer to another. The superposition of Voigt profiles identified using the method of Zhang et al. seems to reproduce the input spectrum quite well (see Fig. 2 of Zhang et al. 1996), although the agreement has not been carefully quantified. One should keep in mind possible differences in the column density distributions obtained using different methods (see Davé et al. 1997 for related discussions).

We also show in Fig. 5 two sets of curves based on the lognormal approximation but using the same Density-Peak-Ansatz (see Gnedin and Hui 1996). One of them has the

same amount of initial smoothing as that of the truncated Zel'dovich approximation and the other has less smoothing so as to match the final (not linear) rms density fluctuation of the Zel'dovich computation. In both cases, the lognormal approximation tends to predict too much flattening of the column density distribution at low column densities. In general the lognormal approximation tends to give column density distributions that deviate quite significantly from power-law unless a very small smoothing length k_S^{-1} is chosen. (From the figure, it might appear that the lognormal approximation gives more lines than the Zel'dovich approximation at the very low column densities but it is really a resolution effect: see the next sub-section.)

The reader might have noticed that we have included in Fig. 5 a wider range of column densities than is warranted by the nature of our approximations. For instance, objects with column densities higher than 10^{16} cm^{-2} are almost certainly highly nonlinear and we do not expect the truncated Zel'dovich approximation to work well in this regime. For the low column densities, the finite resolution should cause us to underestimate the number of absorption lines. In the next sub-section, we give quantitative estimates of the range of column densities within which the Density-Peak-Ansatz, used in conjunction with the truncated Zel'dovich approximation, can be counted upon to give reliable column density distributions.

We will also discuss two different ways of defining a density peak in the next sub-section: local maxima over three cells or local maxima over five cells with the slope on either side of the maxima not changing signs. The three-cell criterion is used in Fig. 5. One expects however that some of the three-cell peaks are not real but merely artifacts of numerical noise, especially those with low column densities. The five-cell criterion, on the other hand, probably fails to include some narrow peaks which are real. We will see that the two different criteria give almost identical results above a certain column density.

One aspect of the Density-Peak-Ansatz we have glossed over is that two density peaks that are separated by a distance in velocity space much less than the thermal width should be counted as contributing to not two but one absorption line. A more sophisticated approach would be to group together such density peaks and use the sum of their column densities as the column density of one single absorption line. We find that for the the range of validity discussed in the following sub-section, it makes little difference. It is conceivable, however, that this effect cannot be ignored for simulations with higher resolution than we have, or at higher redshifts, where line blending is more important.

5.2. The Range of Validity

For the computation presented in Fig. 5, the column density (given by the Density-Peak-Ansatz) above which the mean δ_b exceeds 5 is about $10^{14.1} \text{ cm}^{-2}$. For the parameters listed in the caption of Fig. 5, $N_{\text{HI}} = 3.6 \times 10^{13} A \text{ cm}^{-2}$ (eq. [27]). We therefore take $A = 3.5$ as an upper limit beyond which we cannot expect our approximations to be reliable. Shock-heating should be relatively unimportant for δ_b less than about 5 (see Hui & Gnedin 1996).

Note that according to Fig. 5, comparing with the hydrodynamic simulation data, the Density-Peak-Ansatz coupled with the truncated Zel'dovich approximation, seems to give a reliable number density of absorption lines even for column densities higher than $10^{14.1} \text{ cm}^{-2}$. The level of agreement at such high column densities (and by extension, such high δ_b) is surprising. We will adopt the conservative upper limit of $A = 3.5$.

To determine the column density below which finite resolution results in an underestimate of the number of absorption lines, we perform a simulation using the truncated Zel'dovich approximation with the same parameters as the open squares in Fig. 5 but higher resolution: same box size of 12.8 Mpc but smaller grid spacing of 0.0284 Mpc. A comparison of the resulting column density distributions is made in Fig. 6.

Note that we have included two definitions of density peaks (three-cell and five-cell). For each simulation, the true column density distribution is probably somewhere between the two in the places they differ.

We take the low column density cut-off to be $10^{12.8} \text{ cm}^{-2}$ for the lower resolution simulation (box size of 12.8 Mpc, with grid spacing of 0.05 Mpc) using the three-cell definition of peaks. It can be seen that the higher resolution simulation differs from the lower one only at column densities less than roughly this cut-off value. Moreover, above this column density, the three-cell and five-cell criteria give almost identical results.

The parameters in the simulations in Fig. 6 are such that $N_{\text{HI}} = 3.6 \times 10^{13} A \text{ cm}^{-2}$ (eq. [27]). Hence the above column density cut-off implies a lower limit of 0.18 for A . From now on, we will use the three-cell definition of density peaks.

For readers interested in applying our formalism at different redshifts, we recommend that they choose the appropriate range of A using the same methods above: upper limit set by non-linearity and lower limit set by running simulations of varying resolutions. The range is not expected to change significantly with redshift.

In the following section, we systematically investigate how the column density distribution depends on the cosmological parameters and properties of the intergalactic

medium. All the simulations presented in the next two sections have the same resolution and box size, 256^3 grid points with grid spacing of 0.05 Mpc. For each of them, we will only plot the part of the column density distribution that falls within the limits of $0.18 < A < 3.5$. The column densities these limits correspond to depend on the properties of the intergalactic medium and the redshift (eq. [27]). Note that our conservative limits for A greatly reduce the range of column densities we can examine, but within these limits we can be reasonably confident that the truncated Zel'dovich approximation together with the Density-Peak-Ansatz should yield accurate predictions for the column density distribution.

6. The Column Density Distribution: Dependence on the Ionization Flux, Temperature, Equation of State and the Mean Baryon Density

We use the Cold Dark Matter (CDM) model presented in Fig. 5 to study systematically how the column density distribution depends on properties of the intergalactic medium: the level of radiation background, the mean baryon density and its thermal properties. The tools we use to calculate the column density distributions are the truncated Zel'dovich approximation and the Density-Peak-Ansatz.

The transfer functions for this model and all the other models considered in this paper are taken from Ma (1996). A summary of parameters of all models can be found in Tables 1 and 2.

6.1. Dependence on Overall Temperature, Ionization Flux and Baryon Density

Let us first consider the case in which the equation of state is fixed at $T \propto (1 + \delta_b)^{0.5}$. As is shown in equation (27), the column density of a density peak with a given δ_b (overdensity) is proportional to the following combination of parameters:

$$F \equiv \left(\frac{T_0}{10^4 K} \right)^{-0.7} \left(\frac{\Omega_b h^2}{0.0125} \right)^2 \left(\frac{J_{\text{HI}}}{0.5} \right)^{-1}. \quad (32)$$

Hence, by equation (30), if F is rescaled by a certain factor (by changing T_0 , Ω_b or J_{HI} or their combinations), the number of absorption lines is also changed by the same factor at an appropriately rescaled column density.

Suppose F is rescaled to F' such that $F' = rF$, then

$$\left. \frac{d^2 N'_{\text{Ly}\alpha}}{dN'_{\text{HI}} dz} \right|_{N'_{\text{HI}}=rN_{\text{HI}}} = \frac{1}{r} \left. \frac{d^2 N_{\text{Ly}\alpha}}{dN_{\text{HI}} dz} \right|_{N_{\text{HI}}}. \quad (33)$$

It implies that if the column density distribution is a pure power law, then in a log-log plot of the number of absorption lines per unit column density per unit redshift versus column density, the straight line would simply be shifted to the right or left (or up/down) by rescaling. In reality, the column density distribution only approximately obeys a power law and so there should be a slight change of slope at any given column density as a result of rescaling.

The effects of rescaling can be seen clearly in Fig. 7, where F is allowed to take the values 0.25, 1 and 5. Keeping $\Omega_b h^2 = 0.0125$ and $J_{\text{HI}} = 0.5$, it corresponds to changing T_0 from about 72000 K to 1000 K. Alternatively, keeping T_0 and $\Omega_b h^2$ fixed at their canonical values (as shown in eq. [32]), it corresponds to allowing J_{HI} to vary between 2 and 0.1. See Hui and Gnedin (1996) for a discussion of the dependence of T_0 on reionization history. T_0 is expected to fall within the range quoted above.

The conventional value of $\Omega_b h^2 = 0.0125$ has been challenged by recent measurements of light element abundance in high redshift absorption systems. Tytler and Burles (1996) obtain a value of 0.024, which for $T_0 = 10^4$ K and $J_{\text{HI}} = 0.5$, implies $F = 3.686$, well within the range of F plotted in Fig. 7. The analysis of Rutgers and Hogan (1996), on the other hand, favors the value 0.006, which means $F = 0.23$ for the same values of T and J_{HI} . The lowest set of points in Fig. 7 has to be lowered further to accommodate this value of the baryon density.

The observational data are taken from Hu et al. (1995), measured at about redshift of 3 and corrected for incompleteness. The incompleteness correction was obtained by applying the same spectral analysis technique for the observed data to simulations of randomly distributed Voigt-profiles with a known column density distribution and measuring how much the analysis method underestimates the number of low column density lines. The amount ranges from about no correction necessary at $N_{\text{HI}} > 2 \times 10^{13} \text{ cm}^{-2}$ to a factor of 5 increase in the number of lines at $N_{\text{HI}} \sim 3 \times 10^{12} \text{ cm}^{-2}$.

We note in passing that strictly speaking, altering Ω_b , in addition to rescaling the number of absorption lines as discussed above, also changes the transfer function in a non-trivial way. But the effect is very small for models in which the dark matter (non-baryons) dominate. In fact, using the BBKS (Bardeen et al. 1986) transfer function, which does not take into account the effect of baryons at all, instead of the Ma (1996) transfer function, which does take it into account for $\Omega_b h^2 = 0.0125$ with $h = 0.5$, gives essentially the same column density distribution for the range of column densities discussed here. For models where the baryon content is proportionally higher, Low-density Cold Dark Matter Models for instance, changing $\Omega_b h^2$ has a more pronounced effect on the transfer function.

6.2. Dependence on the Equation of State or the Temperature-density Relation

Let us hold fixed T_0 , $\Omega_b h^2$ and J_{HI} at their canonical values as shown in equation (32) but allow the equation of state to change, for the same CDM model as above. As is pointed out in Sec. 3.2, the temperature-density relation for low enough overdensity is well-approximated by a power law where the power index is around 0.5, but can change slightly depending on the reionization history. We plot in Fig. 8 the column density distributions for $\gamma = 1.2, 1.5, 1.7$ where γ is defined by $T \propto (1 + \delta_b)^{\gamma-1}$. It should adequately cover the possible range of γ (Hui & Gnedin 1996).

The first thing to notice is that the column density distribution remains almost the same for the three different values of γ . This is because γ affects column density through the power index of $(1 + \delta_b)$, which is $2 - 0.7(\gamma - 1)$ (eq. [28]). The index does not change significantly for the range of γ considered. A larger index (smaller γ) means for a density peak with a given $1 + \delta_b$ (and its second derivative), the column density is larger or smaller depending on whether $1 + \delta_b$ is bigger or smaller than one. The net effect is to decrease the slope of the column density distribution. The effect, though very small for the values of γ plotted, can still be seen in Fig. 8. We also show the approximate slopes given by an analytical formula (eq. 41) which will be discussed later. Note how the column density distribution does not exactly follow a power law but can be approximated by one.

Hence as a crude approximation, we conclude that the mean temperature, radiation intensity and baryon density mainly determine the overall normalization of the column density distribution. The equation of state, on the other hand, mostly affects the slope of the column density distribution, but its effect is small for a reasonable range of γ .

7. The Slope of the Column Density Distribution

It has been shown that the normalization of the column density distribution is influenced by the thermal and ionization states of the intergalactic medium, which are not well-constrained observationally. The slope of the distribution, on the other hand, is only weakly affected by the equation of state or temperature-density relation.

The slope of the column density distribution is therefore relatively free of uncertainties due to our ignorance of the thermal and ionization properties of the intergalactic medium. We now turn our attention to the effect of the power spectrum on the slope of the distribution.

From equations (27) and (28), it can be seen that the column density N_{HI} is proportional to $(1 + \delta_b)^{2-0.7(\gamma-1)}$ times $1/\sqrt{\xi''}$, which basically defines a length scale. Taking into account the correlation between this length scale and the overdensity, we find from our simulations (which use the Zel'dovich approximation) a useful approximate relation for column densities between about $10^{12.5}$ and $10^{14.5} \text{ cm}^{-2}$ (or more accurately, for the range of validity discussed in Sec. 5.2):

$$N_{\text{HI}} \propto (1 + \delta_b)^{1.68-0.7(\gamma-1)}, \quad (34)$$

which roughly means the length scale $1/\sqrt{\xi''}$ is approximately proportional¹² to $(1 + \delta_b)^{-0.32}$.

Since we are interested in the slope of the column density distribution, the relevant quantity to consider is:

$$-\beta \equiv \frac{d \ln \frac{d^2 N_{\text{Ly}\alpha}}{d N_{\text{HI}} dz}}{d \ln N_{\text{HI}}} = -1 + \frac{m}{1.68 - 0.7(\gamma - 1)}, \quad m \equiv \frac{d \ln \int_{-\infty}^0 d\xi'' |\xi''| P(\xi, \xi' = 0, \xi'')}{d\xi}. \quad (35)$$

The equality follows from equations (34), (27), (30) and (31) and noting that $\xi \equiv 1 + \delta_b$. The column density distribution can be approximated by the simple power law $N_{\text{HI}}^{-\beta}$ if β defined above is only weakly dependent on ξ or N_{HI} .

Lacking an analytical expression for P under the Zel'dovich approximation, we can nonetheless guess what the general properties of the quantity m are. First of all, m depends on ξ in general because the integral $\int_{-\infty}^0 d\xi'' |\xi''| P(\xi, \xi' = 0, \xi'')$ cannot be a simple power law in ξ . This is because we expect the integral to vanish for very large and very small ξ and peak at some intermediate ξ . This implies one should not expect an exact power-law for the column density distribution, although pieces of it might be approximated by power-law. Suppose ξ_{pk} is the value of ξ where the integral $\int_{-\infty}^0 d\xi'' |\xi''| P(\xi, \xi' = 0, \xi'')$ reaches its maximum value, then the column densities we are interested in must correspond to $\xi > \xi_{\text{pk}}$ where $d \ln \int_{-\infty}^0 d\xi'' |\xi''| P(\xi, \xi' = 0, \xi'')/d\xi$ is negative. This is based on the knowledge that the computed (as well as observed) slope in equation (35) is less than -1 (the factor $1.68 - 0.7[\gamma - 1]$ is always positive for reasonable values of γ).

Under the Zel'dovich approximation, the quantities ξ and its derivatives can be related to the displacement potential $\psi(\mathbf{q})$ using equations (11) and (12) and so one can express $P(\xi, \xi', \xi'')$ in terms of the probability density for derivatives of ψ :

$$\int_{-\infty}^0 d\xi'' |\xi''| P(\xi, \xi' = 0, \xi'') = \int_{\infty}^0 d\xi'' d\psi_{ij} d\psi_{ijk} d\psi_{ijkl} |\xi''| e^{-\xi} P(\psi_{ij}, \psi_{ijk}, \psi_{ijkl}) \delta_D[\xi - \xi(\psi_{ij})] \delta_D[\xi'(e^i, \psi_{ij}, \psi_{ijk})] \delta_D[\xi'' - \xi''(e^i, \psi_{ij}, \psi_{ijk}, \psi_{ijkl})], \quad (36)$$

¹²A log-log plot of $1/\sqrt{\xi''}$ versus $(1 + \delta_b)$ actually shows a lot of scatter but equation (34) appears to capture the overall dependence of N_{HI} on $1 + \delta_b$.

where δ_D denotes the Dirac delta function, ψ_{ij} is the derivative of the displacement potential ψ with respect to q_i and q_j (eq. [11]) and similarly for ψ_{ijk} and ψ_{ijkl} and e^i is the unit vector pointing along the line sight. The quantity $P(\psi_{ij}, \psi_{ijk}, \psi_{ijkl})$ is the probability density of ψ_{ij} and its derivatives in Lagrangian space and the factor $e^{-\xi}$ converts it into its counterpart in Eulerian space (see Kofman et al. 1994). The quantities ξ and its derivatives along the line of sight can be expressed as functions of ψ_{ij} , ψ_{ijk} , ψ_{ijkl} and e^i . Isotropy of the universe implies that one can average the above expression over all possible orientations of e^i .

For the cosmological models we consider in this paper, the probability density $P(\psi_{ij}, \psi_{ijk}, \psi_{ijkl})$ is a multivariate Gaussian function that depends on 3 parameters: σ_0 , σ_1 and σ_2 defined as follows (see Bardeen et al. 1986):

$$\sigma_j = D_+(t) \sqrt{\int_0^\infty 4\pi k^{2+2j} P(k) e^{-(k/k_S)^2} dk}, \quad j = 0, 1, 2 \quad (37)$$

where D_+ is the linear growth factor which is equal to $(1 + \bar{z})^{-1}$ for a universe at critical matter density and k_S is an appropriate smoothing scale. This follows from the structure of the various expectation values: $\langle \psi_{ij} \psi_{mn} \rangle \propto \sigma_0^2$, $\langle \psi_{ij} \psi_{mnl} \rangle \propto \sigma_1^2$, $\langle \psi_{ijkl} \psi_{mnop} \rangle \propto \sigma_2^2$ and $\langle \psi_{ijk} \psi_{mnl} \rangle \propto \sigma_1^2$. The fact that $\langle \psi_{ij} \psi_{mnl} \rangle$ and $\langle \psi_{ijkl} \psi_{mno} \rangle$ vanish by isotropy means that the probability density factors into two separate multivariate Gaussian functions: $P(\psi_{ij}, \psi_{ijk}, \psi_{ijkl}) = P(\psi_{ij}, \psi_{ijk})P(\psi_{ijkl})$, with the first factor depending on σ_0 , σ_1 and σ_2 and the second factor depending on σ_1 .

One can replace σ_1 and σ_2 by combinations of σ_0 and the following two new parameters, which Bardeen et al. (1986) defined:

$$R_* \equiv \sqrt{3} \frac{\sigma_1}{\sigma_2}, \quad \gamma_B \equiv \frac{\sigma_1^2}{\sigma_2 \sigma_0}, \quad (38)$$

where we have renamed γ_B to distinguish it from γ we use in this paper.

While R_* defines a length scale, the quantity γ_B is a measure of the slope of the power spectrum. We find it convenient to use the following quantity n_{eff} in place of γ_B (Bardeen et al. 1986):

$$n_{\text{eff}} \equiv \frac{5\gamma_B^2 - 3}{1 - \gamma_B^2}. \quad (39)$$

It is easy to show that the above quantity coincides exactly with the slope of the power spectrum if it obeys a pure power-law. For $\gamma_B = 0.5$, $n_{\text{eff}} = -2.33$. The n_{eff} defined here should be distinguished from n in Tables 1 and 2: n is the slope of the power spectrum at large scales whereas n_{eff} is the slope at the (small) smoothing scale.

The advantage of the new notation is that it is possible to show, by changing variables $\bar{\psi}_{ijk} \equiv \psi_{ijk} R_*$, $\bar{\psi}_{ijkl} \equiv \psi_{ijkl} R_*^2$ and $\bar{\xi}'' = \xi'' R_*^2$, the integrals in equation (37) are independent

of R_* except for a normalization factor. This implies, by equations (35) and (37), that the slope β depends on the equation of state through γ and on the power spectrum only through σ_0 and n_{eff} .

It is hard to make analytic progress from this point on, because ξ and its derivatives are complicated functions of the derivatives of ψ . We resort to our numerical simulations to extract the parameter dependence of β . Using the above arguments and observing that for all models we consider in this paper, $\sigma_0 \sim 1$ and $n_{\text{eff}} \sim -2.33$ ($\gamma_B \sim 0.5$), we assume the following form for β :

$$\beta = 1 + \frac{B_1 + B_2(\sigma_0 - 1) + B_3(n_{\text{eff}} + 2.33)}{1.68 - 0.7(\gamma - 1)}, \quad (40)$$

where B_1 , B_2 and B_3 are constant coefficients of a Taylor series expansion of m (eq. [35]).

We determine these constants by computing β for a series of CDM models of varying σ_0 and γ_B . The column density distributions are obtained by using the Zel'dovich approximation together with the Density-Peak-Ansatz, as described in previous sections. We pick out particularly models with similar n_{eff} 's but very different σ_0 's and vice versa. It is found that the following expression for β fits reasonably well the slope of the column density distributions for the CDM models, as well as the Cold + Hot Dark Matter (CHDM) models that we will also study later:

$$\beta = 1 + \frac{0.96 - 0.8(\sigma_0 - 1) - 0.4(n_{\text{eff}} + 2.33)}{1.68 - 0.7(\gamma - 1)}, \quad (41)$$

where β , γ , σ_0 and n_{eff} are defined in equations (35), (19), (37) and (39) respectively.

We show two sets of examples in Fig. 9 and Fig. 10. The former has two CDM models with the same n_{eff} but different σ_0 's while the opposite is true for the latter. To find models with such properties, we find it necessary sometimes to smooth on scales larger than the orbit-crossing scale k_S^{-1} defined by equation (15) (examples are models CDM3 and CDM4 shown in the Figures; see also Table 1). For this reason, the column density distributions computed in this section should be viewed as predictions of the corresponding CDM models at the specified smoothing scales only: they do not necessarily coincide with the predictions of these models if more appropriate smoothing scales are chosen. Nor should the CDM models shown in the two figures be considered realistic models of the universe.

Examples of how well equation (41) describes the variation with the equation of state for a CDM model can be found in Fig. 8. More examples for CHDM models are also shown in Figures 15, 16, 17 and 18.

Before we go on to discuss physical interpretations of the above expression for β , let us make some general remarks and state a few caveats. First, as we discussed before, β

is expected to vary with column density but can be approximated as a constant over a restricted range. That a power-law column density distribution is only an approximation is clear even in some of the figures mentioned above. We find it appropriate to allow for a maximum error-bar of ± 0.1 for β in equation (41), given γ , σ_0 and γ_B . The coefficients B_1 , B_2 and B_3 (eq. [40]) should be viewed as correspondingly uncertain. Furthermore it should be kept in mind that equation (41) holds only for $\sigma_0 \sim 1$ and $n_{\text{eff}} \sim -2.33$, as the constants B_1 , B_2 and B_3 are only meant to be coefficients of a Taylor series expansion.

Finally, one obvious problem of using equation (41) to make prediction for a given cosmological model is that both σ_0 and n_{eff} varies with the smoothing scale. An example of how the choice of smoothing scale can affect the column density distribution is shown in Fig. 11. The comparison between results of a hydrodynamic simulation and our Zel'dovich computation in Fig. 5 seems to support the choice of smoothing in equation (15). However, one could reasonably argue that the Jeans scale (eq. [16]) is a more physically motivated smoothing scale while the choice in equation (15) was made only as a device to counter the effect of orbit-crossing and hence one cannot be sure that one is not thereby erasing real structures on scales smaller than the orbit-crossing scale but larger than the Jeans length, which can contribute significantly to the low column density Lyman-alpha forest. One way to settle this question is to make more detailed comparisons with more hydrodynamic simulations, which is outside the scope of the present work and we will leave for a future paper. It suffices to say that, for models with sufficiently little small scale power such as the CHDM models considered in Sec. 8, which have orbit-crossing scales close to or smaller than the Jeans length, it is probably safe to smooth according to the prescription laid down in Sec. 3.1 and that the precise smoothing scale might not matter very much (see Fig. 13). For more nonlinear models, we can only offer the comparison in Fig. 5 as one piece of evidence that smoothing on the orbit-crossing scale works reasonably well. However, for whatever smoothing scale one decides upon, we expect equation (41) to hold approximately, provided that $\sigma_0 \sim 1$ and $n_{\text{eff}} \sim -2.33$.

With these being said, let us try to understand qualitatively the parameter dependence of β as expressed in equation (41).

First, the dependence on γ . Recall that $N_{\text{HI}} \propto (1 + \delta_b)^{1.68 - 0.7(\gamma-1)}$ (taking into account the correlation between $1 + \delta_b$ and its second derivative). This means that higher density peaks translate into higher N_{HI} and vice versa. Lowering γ increases the effect of this translation i.e. a given density peak with $1 + \delta_b > 1$ is associated with a higher column density if γ is reduced (the opposite is true for $1 + \delta_b < 1$). The net effect is to stretch a power-law-like column density distribution and make it flatter. The effect is small for a reasonable range of γ . It should be between 1.3 and 1.62 at $\bar{z} = 3$ if the universe reionizes

before $\bar{z} \sim 5$ (see Hui and Gnedin 1996). A somewhat larger range is shown in Fig. 8.

Second, the dependence on σ_0 : a cosmological model with lower σ_0 is in a more “linear” state of evolution compared to higher σ_0 models. In other words, a lower σ_0 model has proportionally more intermediate density peaks compared to high density ones, hence the steeper column density distribution (associating once again high density peaks with high column densities using the $N_{\text{HI}} \propto (1 + \delta_b)^{1.68 - 0.7(\gamma-1)}$ scaling). For sufficiently low column densities, however, the absorption lines arise from very underdense regions which should be more common in higher σ_0 models. Hence at very low column densities, the high σ_0 model should win: it has more very low density peaks. Where this might occur we cannot tell from our simulations because of the limited resolution. For the range of column densities we can measure reliably, the slope of the column density distribution simply steepens as σ_0 is lowered.

The dependence of β on n_{eff} is more subtle. To understand it, we resort to a Press-Schechter-type argument (Press & Schechter 1974). According to the Press-Schechter theory, the low mass slope of $n_C(M)$ (the number density of clumps of mass M per unit range dM) is $-1.5 + n_{\text{eff}}/6$ which means that smaller n_{eff} ($n_{\text{eff}} < -1$) implies a steeper slope of the clump number density distribution, exhibiting the same trend as in the case of equation (41). The n_{eff} dependence arises from the fact that $\sigma_0(k) \propto k^{(n_{\text{eff}}+3)/2}$ (σ_0 with smoothing scale k) and assuming $M \propto k^{-3}$, together with $Mn_C(M) \propto k^3/\sigma_0(k)$ (for high k). The factor of k^3 appears because $n_C(M)$ is a number density. The dependence of $n_C(M)$ on $\sigma_0(k)$ follows from a simple conjecture: the probability that a given point belongs to a clump of mass M or higher is equal to $2 \int_{\delta_{\text{th}}}^{\infty} P(\delta) d\delta$ where δ_{th} is a fixed threshold and $P(\delta)$ is the Gaussian probability distribution for overdensity δ with dispersion $\sigma_0(k)$.

One can carry the above reasoning over to absorption lines, keeping in mind something like the Threshold Algorithm for identifying lines as the analogue of the threshold-criterion of the Press-Schechter theory for a collapsed clump. Assume $N_{\text{HI}} \propto k^{-1}$ (because in the linear regime, it is the peak width, not the peak height that provides the lowest order contribution to column density), it “follows” that $N_{\text{HI}}(d^2 N_{Ly\alpha}/dN_{\text{HI}} dz) \propto k/\sigma_0(k)$, again in the high k limit. The factor of k is to account for the quantity of interest being a one-dimensional number density. It is easy to see this implies $\beta = (1 - n_{\text{eff}})/2$ i.e. smaller n_{eff} (larger $|n_{\text{eff}}|$) implies steeper column density distribution. This admittedly crude argument actually gives a value for β that agrees surprisingly well with what we have found using the Zel'dovich approximation and Density-Peak-Ansatz. For example, for the CDM model in Fig. 5, $n_{\text{eff}} = -2$ (see Table 1), $\beta = 1.5$ according to the adapted-Press-Schechter argument. This of course brings up the question why there does not seem to be any σ_0 dependence of β in the above argument. It is in fact possible to develop this line of

reasoning further to include the σ_0 dependence, but we will leave this to a later paper.

Finally, it is interesting to point out that because most realistic cosmological models have similar power on large scales (COBE or cluster scale), small σ_0 on small scales almost necessarily means a steeper fall-off of the power spectrum, namely smaller n_{eff} . So, in practice, both the amplitude σ_0 and the slope n_{eff} of the power spectrum work in the same direction in decreasing/increasing the slope of the column density distribution. Hence, as a rule of thumb, less small scale power implies a steeper column density distribution, for the column densities of interest in this paper.

8. The Column Density Distribution for CHDM models

In this section, we turn our attention to CHDM models, which have relatively little small scale power and for which the method of truncated Zel'dovich approximation is ideally suited. The orbit-crossing scales for them are either smaller than or only slightly larger than the Jeans length and so one has reasons to believe any structure erased by our smoothing procedure does not contribute significantly to the number of absorption lines in the range of column densities we are interested in. Predictions for the CHDM models are also of current interest because no hydrodynamic simulations of the Lyman-alpha Forest have been performed for these models.

We list in Table 2 the CHDM models considered in this section. They are all $\Omega_0 = 1$ models with $\Omega_b = 0.05$. Both the $\Omega_\nu = 0.2$ and $\Omega_\nu = 0.1$ versions are considered. They have been shown to give good agreement with the observational data on large scales (k around $0.02 - 0.4 \text{ Mpc}^{-1}$) (see Fig. 6 and 7 of Ma 1996). The $\Omega_\nu = 0.3$ models seem to conflict with the observed abundance of damped Ly α systems, which correspond to roughly k around $0.1 - 1.0 \text{ Mpc}^{-1}$ comoving in the linear power spectrum (Mo & Miralda-Escudé 1994; Kauffmann & Charlot 1994; Ma & Bertschinger 1994). We include one $\Omega_\nu = 0.3$ CHDM model in Table 2 for the sake of comparison. As is shown convincingly by Ma (1996), all models need some amount of tilt to match observations.

We compute as before the column density distribution for each model using the Density-Peak-Ansatz and the Zel'dovich approximation with appropriate smoothing. The (density weighted) power spectrum for each CHDM model is taken from Ma (1996).

As we have discussed in the last section, a plot of rms smoothed linear density fluctuation σ_0 versus smoothing scale k_S (eq. [37]) is a very good indicator of what column density distribution to expect. This is done in Fig. 12 for the CHDM models tabulated in Table 2. The no-tilt $\sigma_8 = 0.7$ CDM model is also plotted for comparison.

Because of neutrino free streaming, all CHDM models have less power (smaller σ_0) and steeper spectral slope (smaller n_{eff}) than the CDM model on small scales. Those with more neutrino content ($\Omega_\nu = 0.2$) have even less power than the others. In fact, the $\Omega_\nu = 0.2$ models have $\sigma_0 < 1$ on all scales larger than the Jeans scale ($k_S < k_J \sim 10 \text{ Mpc}^{-1}$). One expects the Zel'dovich approximation to work particularly well for these models because the amount of orbit-crossing will not be significant, even without initial truncation.

This is borne out by the next test: we compute the column density distribution for one CHDM model B2 and examine the effect of choosing different smoothing scales. The result is plotted in Fig. 13. The column density distribution in the range plotted does not change much at all for the three different smoothing scales plotted. Contrast this with the case of $\sigma_8 = 0.7$ CDM (Fig. 11) where the column density distribution is more sensitive to changes in the smoothing scale. That's why the truncation scale has to be chosen with some care for the CDM model: not too small (k_S too big) so that too much orbit crossing has occurred and not too large so that too much small scale structure is erased. The standard prescription (Sec. 3.1) seems to work well according to Fig. 5.

For the CHDM model considered (in fact, it holds true for all other $\Omega_\nu = 0.2$ models here), the amount of small scale power is so insignificant that excluding them by smoothing does not affect the overall column density distribution at all (except possibly that one loses the small scale fluctuations that can give rise to very low column density absorption i.e. lower than our resolution limit). We have also done similar tests for the $\Omega_\nu = 0.1$ models, their response to changes in the truncation scale is somewhere between the $\sigma_8 = 0.7$ CDM model and the $\Omega_\nu = 0.2$ CHDM models, as can be expected based on their difference in Fig. 12.

We adopt the following truncation scales for the CHDM models. For the $\Omega_\nu = 0.1$ models, the standard prescription described in Sec. 3.1 is used (i.e. $k_S = 1.5 k_{\text{NL}}$). The $\Omega_\nu = 0.2$ models, according to the above prescription, would have truncation scales less than the Jeans length ($k_S > k_J$) and so by the arguments presented in Sec. 3.1, $k_S = k_J$ is adopted. Again, we emphasize that for this class of models that have relatively little power on small scales, the precise truncation scale is not important. A summary of the truncation scales for all models can be found in Table 2.

The CHDM models with $\Omega_\nu = 0.1$ are plotted in Fig. 14. Values of F that give reasonable match to the observational data are chosen for each model. Note how the low-Hubble-constant-models ($h = 0.5$) require a slightly lower F (eq. [32]) than the higher-Hubble-constant-models. The equation of state is chosen to be the same for all models ($\gamma = 1.5$, see equation [19]). The level of agreement with the observational data, for the given choices of parameters, is satisfactory. Notice how the low Hubble-constant

($h = 0.5$) models tend to have steeper column density distributions, because they have less power on the relevant scales (see Fig. 12). Their slopes can be brought into better agreement with that of the observational data if a smaller γ is used.

For the $\Omega_\nu = 0.2$ models, we cannot find values of F that give the same level of agreement with observations for $\gamma = 1.5$. Two examples are shown in Fig. 16 and Fig. 15. Both have $h = 0.5$ and small amounts of tilt. For each, three sets of theoretical predictions are plotted, one for each value of F : 1, 2.5 or 5. For $\Omega_b h^2 = 0.0125$, the conventional Big-bang nucleosynthesis value, and $T_0 = 10^4$ K, they correspond to radiation intensity J_{HI} of 0.5, 0.2 and 0.1 (eq. [32]). As we have shown before, changing F mainly shifts the sets of points without altering the slope significantly. For the column density between about $10^{12.5}$ and $10^{14.5}$ cm $^{-2}$, the slope of the predicted distribution seems to be too steep compared to the observational data. β is about 1.86, with some flattening at the lower column densities, compared with the observed value of about 1.5.

Another $\Omega_\nu = 0.2$ CHDM model (*D2* in Table 2), which has a higher Hubble constant ($h = 0.65$), is shown in Fig. 17. (The *C2* CHDM model which also has $h = 0.65$, gives very similar column density distribution.) The slope of its column density distribution is not as steep as the previous ones. This is expected because the higher Hubble constant models have slightly more power on relevant scales, as is evident in Fig. 12. In fact, one might argue that the middle set of points in Fig. 17, the one having $F = 3.57$, matches the observational data reasonably well if both observational and theoretically errors are carefully taken into account. However, it is still true these two models predict a steeper column density distribution for N_{HI} between about $10^{12.5}$ and $10^{14.5}$ cm $^{-2}$, compared to the $\Omega_\nu = 0.1$ CHDM models (Fig. 14).

It is not hard to understand the column density distributions of the CHDM models presented if one refers back to Fig. 12 or Table 2. The $\Omega_\nu = 0.2$ models have less power (smaller σ_0) and steeper spectral slope (larger $|n_{\text{eff}}|$) than those with $\Omega_\nu = 0.1$ on scales $1\text{Mpc}^{-1} \lesssim k_s \lesssim 10\text{Mpc}^{-1}$, which are relevant for the range of column densities we are interested in. As we have explained before, the column density distributions are therefore steeper for the $\Omega_\nu = 0.2$ models at this range of column densities. Among the $\Omega_\nu = 0.2$ models, those with a lower Hubble constant produce comparatively steeper column density distributions because they have even less small scale power and steeper spectral slope than the ones with a higher Hubble constant.

In discussing the predictions of the slope of the column density distribution for these models, one should bear in mind uncertainties due to the choice of smoothing scale, as we have presented in the last section. However, the fact that these CHDM models have relatively little power on small scales works in our favor: the exact choice of the smoothing

scale does not affect the slope of the distribution very much (see Fig. 13). This is especially true for the $\Omega_\nu = 0.2$ models which have orbit-crossing scales (eq. [15]) smaller than the Jeans length. So, the general conclusion of steeper column density distribution for the tilted CHDM models considered here compared to, say, the CDM1a model (see Table 1 and Fig. 5; the results of which compare favorably with a hydrodynamic simulation) should be robust.

In Sec. 6, we have discussed how the equation of state or temperature-density relation can also change the slope of the column density distribution, although the effect is small for a reasonable range of γ . We show in Fig. 18 the effects of altering the equation of state on the column density distribution for one particular CHDM model (*A2*). F is fixed at 2.5, the value that seems to give a column density distribution closest to the observational data. Smaller γ , as we have noted before, helps flatten the column density distribution but the flattening seems to be not quite enough even for $\gamma = 1.2$. We show in the same figure a dashed line with a slope of -1.75 (which follows from equation (41) by putting $\gamma = 1.2$ and substituting the appropriate values of σ_0 and n_{eff} as given in Table 2). It should be kept in mind that we can always shift the column density distribution up and down by rescaling F (Sec. 6), so the normalization is not important. It seems $\gamma < 1.2$ is needed for this model to give the right slope of the distribution, at least the right slope to within the 95% confidence limits of the observed β (1.37, 1.51). The same conclusion holds for the other low Hubble constant $\Omega_\nu = 0.2$ model (*B2*). We should emphasize, however, that a more detailed comparison between the predictions of the models and observations, taking into account noise and biases of the line identification techniques, is necessary before any model can be considered ruled out.

The high Hubble constant ($h = 0.65$) $\Omega_\nu = 0.2$ models *C2* and *D2*, on the other hand, have intrinsically flatter distributions and a reasonable match between theory and observations can be made by choosing γ in the range 1.2 – 1.7.

9. Conclusion

We have systematically developed a set of tools to compute in an efficient manner the column density distribution given a cosmological model. One fundamental assumption of the approximations involved is that most of the Ly α forest with column densities in the range $10^{12.5} - 10^{14.5} \text{ cm}^{-2}$ originates from regions of low overdensities or even underdensities which have not undergone orbit-crossing. The result of a comparison with a hydrodynamic simulation lends support to it.

One major conclusion we reach, in the process of developing the tools, is that the peculiar velocities play a minor role in determining the column density distribution at our column densities of interest, even though they are very important in determining the shapes of individual absorption line profiles. We take advantage of this fact and develop a method we call the Density-Peak-Ansatz in which each density peak is identified as an absorption line and assigned a column density based on its local properties. The column density distribution then becomes a statistic of density peaks.

In Sec. 6 and 7, we investigate the factors controlling the column density distribution, which can be divided into two categories. One mostly affects the normalization, while the other mostly influences the slope. Those that fall into the former category include the ionizing radiation intensity, the mean temperature of the intergalactic medium and the mean baryon density. Uncertainties in their values are such that almost any viable cosmological model which has the correct slope of the column density distribution can be made to match observations by a judicious choice of parameters.

The factors that mostly affect the slope of the distribution include the equation of state and more strongly so, the amplitude and slope of the (linear) power spectrum on scales $1 \text{ Mpc}^{-1} \lesssim k \lesssim 10 \text{ Mpc}^{-1}$. Models that have less power on these scales tend to have comparatively more intermediate density peaks than high density ones and hence have relatively steeper column density distributions. Models with a steeper power spectrum on these scales have $k^2/\sigma_0(k)$ that falls off more quickly with increasing k^{-1} ($\sigma_0(k) \propto k^{(n_{\text{eff}}+3)/2}$) and therefore a steeper column density distribution, assuming high column density corresponds to high k^{-1} (Press-Schechter argument; see Sec. 7). Equations of state which are closer to isothermal (smaller γ where γ satisfies $T \propto (1 + \delta_b)^{\gamma-1}$) tend to produce flatter column density distributions. However, within the reasonable range of γ (see Hui and Gnedin 1996), its precise value depending upon the reionization history, the effect of changing the equation of state is small. We put forward an approximate expression relating the slope of the column density distribution to γ and the amplitude (σ_0) and slope (n_{eff}) of the power spectrum on small scales (eq. [41]), which describes reasonably well all the models we study in this paper.

Hence, the slope of the column density distribution provides a measure of the amplitude and slope of the power spectrum on small scales for a given cosmological model and given temperature-density relation. We apply our techniques to study a class of CHDM models which are known to have less power on small scales compared to other popular CDM models. We conclude that the CHDM models indeed produce steeper column density distributions compared to the CDM models. In particular, the low Hubble constant ($h = 0.5$) $\Omega_\nu = 0.2$ CHDM models, which have the least amount of power on small scales among the models we

study, have column density distributions which can be made consistent with observations only for γ less than the values we consider reasonable. We emphasize however that only after a more detailed comparison between theories and observations, including all the effects of noise and biases of the line-identification methods, can any model be considered ruled out by the observed column density distribution.

We therefore conclude that a lot of work still needs to be done both on the observational and theoretical fronts. The biases of the line-identification techniques used for data reduction deserve close study so that the error bars in the observed column density distributions can be better understood and perhaps reduced. Numerical simulations on the CHDM models should be carried out to further test the accuracy of the approximations made in the present work. Detailed comparisons with hydrodynamic simulations will shed light on the appropriate choice of smoothing scales for approximate methods such as the one we present here. The effect of a fluctuating radiation field, instead of a uniform one as is assumed here, has to be investigated. Moreover, in terms of constraining models, it is also important to examine other possible statistics. We have shown, for instance, that the column density distribution is relatively independent of peculiar velocities. Are there other statistics that can take advantage of the different peculiar velocity structures predicted by different cosmological models?

In short, the study of the Ly α forest has entered an exciting stage. There is a gold mine of information contained in the quasar absorption spectra waiting to be discovered.

We would like to thank Edmund Bertschinger for his encouragement and many insightful suggestions which greatly improved the paper. We are also grateful to Jeremiah Ostriker for his helpful comments. It is a pleasure to thank Thomas Buchert, Lars Hernquist, Fred Rasio, Ur \ddot{o} s Seljak and Matias Zaldarriaga for useful discussions and Esther Hu for kindly sending us her data on the column density distribution. We thank HongGuang Bi and Arthur Davidsen for correspondence regarding their preprint and we gratefully acknowledge useful comments from Edward Wright. We are indebted to our referee, David Weinberg, for many thoughtful comments and interesting discussions, particularly relating to Sec. 7. This work is supported in part by funds provided by the U.S. Department of Energy (D.O.E.) under cooperative research agreement DE-FC02-94ER40818 and in part by NSF grant AST-9318185 and NASA grant NAG5-2816.

A. Smoothing at Jeans Scale

The effect of gas pressure is to smooth the baryon density field compared to its dark matter counterpart. The length scale below which this becomes important is the Jeans scale. In linear theory, the baryon overdensity obeys the following equation in a dark matter dominated universe (Bi et al. 1992; Peebles 1993):

$$\frac{\partial^2 \tilde{\delta}_b}{\partial t^2} + 2H \frac{\partial \tilde{\delta}_b}{\partial t} = 4\pi G \bar{\rho}_{DM} \tilde{\delta}_{DM} - \frac{\gamma k_B \bar{T}}{\mu a^2} k^2 \tilde{\delta}_b, \quad (A1)$$

where the tilde denotes functions in Fourier space as before, H is the Hubble constant, k_B is the Boltzmann constant, G is the Newton constant, $\bar{\rho}_{DM}$ is the average dark matter mass density, \bar{T} is the average temperature of the gas and μ is the mean mass of each gas particle (for a fully ionized gas composed of hydrogen and helium with primordial abundances, it is about 0.6 times the proton mass). The relation between the temperature (not its average but its actual value) and $1 + \delta_b$ is described by γ , the temperature being proportional to $(1 + \delta_b)^{\gamma-1}$.

The Jeans scale is defined in equation (16). For a dark matter dominated universe, one can replace $\bar{\rho}_{DM}$ by the total mean density of the universe.

For the special case of $\bar{T} \propto a^{-1}$, making use of an equation for $\tilde{\delta}_{DM}$ which is the same as equation (A1) except for the absence of the temperature term, it can be shown that

$$\tilde{\delta}_b(\mathbf{k}) = \frac{\tilde{\delta}_{DM}(\mathbf{k})}{(1 + k^2/k_J^2)}, \quad (A2)$$

if one ignores decaying modes. It expresses in a quantitative way the expectation that the overdensity in baryons is the same as that of dark matter on large scales (low k) but is lower on small scales (high k). For \bar{T} with some other power-law dependence on a , solutions for equation (A1) are more complicated but the low and high k limits are the same: $\tilde{\delta}_b = \tilde{\delta}_{DM}$ for small k and $\tilde{\delta}_b = \tilde{\delta}_{DM} k_J^2/k^2$ for large k (Bi et al. 1992). We note, however, that in practice, the gas temperature is expected to rise from almost zero before reionization to around $10^4 - 10^5$ K after, and so the power-law time-dependence of T is probably not realized. The actual linear smoothing scale of the gas should be a little different from the one given above and one has to be careful about boundary conditions for δ_b and its derivative at the onset of reionization (see Gnedin & Hui 1997).

B. Thermal and Ionization Evolution

The evolution of temperature is governed by:

$$\frac{dT}{dt} = -2HT + \frac{2T}{3(1 + \delta_b)} \frac{d\delta_b}{dt} - \frac{T}{\sum_i \tilde{X}_i} \frac{d\sum_i \tilde{X}_i}{dt} + \frac{2}{3k_B n_b} \frac{dQ}{dt}, \quad (\text{B1})$$

where d/dt is the Lagrangian derivative following each fluid element, n_b is the proper number density of all gas particles and T is the temperature which depends on both space and time. The symbol \tilde{X}_i is defined by $n_i \equiv (1 + \delta_b) \tilde{X}_i \bar{\rho}_b / m_p$, where n_i is the proper number density of the species i , $\bar{\rho}_b$ is the mean mass density of baryons at the time of interest, m_p is the mass of the proton and δ_b is the overdensity as in equation (8). The neutral fraction of hydrogen, X_{HI} (distinct from \tilde{X}_{HI}) as in equation (9), is then $\tilde{X}_{\text{HI}} / (\tilde{X}_{\text{HI}} + \tilde{X}_{\text{HII}})$. Note that \tilde{X}_i is a function of space and time in general.

The first two terms on the right hand side take care of adiabatic cooling or heating. The third accounts for the change of internal energy due to the change in the number of particles. The last term dQ/dt is the heat gain (or negative heat loss) per unit volume by the gas particles from the surrounding radiation field. At a redshift of 2 to 4 and for densities of our interest, the main source of heat gain is photoionization and the main source of heat loss is through the recombination of ionized hydrogen and the free electron. At higher redshifts, other processes become important, such as Compton cooling. More discussion on these processes will be presented in Hui and Gnedin (1996). We note that one particularly simple solution of equation (B1) is $T \propto a^{-2}(1 + \delta_b)^{2/3}$, which holds when the last two terms on the right hand side can be ignored i.e. pure adiabatic expansion or compression.

The above equation has to be supplemented by one that determines the abundance of each particle type, which takes the form:

$$\frac{d\tilde{X}_i}{dt} = -\tilde{X}_i P_h + \sum_{j,k} \tilde{X}_j \tilde{X}_k R \left[\frac{\bar{\rho}_b(1 + \delta_b)}{m_p} \right]. \quad (\text{B2})$$

For instance, if $\tilde{X}_i = \tilde{X}_{\text{HI}}$, P_h is the photoionization rate. It is given by:

$$P_h = \int_{\nu_{\text{HI}}}^{\infty} 4\pi J_{\nu} \sigma_{\text{HI}} \frac{d\nu}{h\nu}, \quad (\text{B3})$$

where h is the Planck constant, $h\nu_{\text{HI}} = 13.6$ eV, σ_{HI} is the cross-section for photoionization as a function of the frequency ν and J_{ν} is the specific intensity. The photoionization rate P_h depends on the normalization as well as spectrum of J_{ν} . The specific intensity J_{ν} is generally taken to have a power law spectrum, ν^{-1} to $\nu^{-1.5}$, for frequencies just above

ν_{HI} . The spectrum at higher frequencies is less important for the photoionization rate of hydrogen. A convenient way to hide our ignorance of the spectrum is to define J_{HI} as in equation (18).

For $\tilde{X}_i = \tilde{X}_{\text{HI}}$, R is the recombination rate of ionized hydrogen and the free electron ($\tilde{X}_j = \tilde{X}_e$ and $\tilde{X}_k = \tilde{X}_{\text{HII}}$ in equation [B2]):

$$R \sim 4 \times 10^{-13} \left(\frac{T}{10^4 K} \right)^{-0.7} \text{cm}^3 \text{s}^{-1}. \quad (\text{B4})$$

For J_{HI} with the values noted in Sec. 3.2, the photoionization time-scale is much shorter than the Hubble time. This means that hydrogen is highly ionized and is essentially in ionization equilibrium. The two terms on the right hand side of equation (B2) almost balance each other, which implies equation (17).

We now have all the equations in place to compute the thermal and ionization evolution. The overdensity δ_b is evolved using the Zel'dovich approximation. Its rate of growth is substituted into equation (B1), which is solved together with equation (B2). The initial conditions are as follows. The gas temperature T is equal to the cosmic microwave background temperature at $z = 100$ (maintained by Compton scattering) and evolves adiabatically after that until the universe is reionized by the UV background. Abundances are assumed to be primordial, which is consistent with observations so far for column densities less than about $10^{14.5} \text{ cm}^{-2}$ (See Songaila and Cowie 1996. Cooling processes due to metals are not important for our densities of interest in any case). All species are neutral until reionization occurs. One can integrate equations (B1) and (B2) forward starting from any time between $z = 100$ and the beginning of reionization to obtain T and \tilde{X}_{HI} or X_{HI} .

REFERENCES

Bagla, J. S., & Padmanabhan, T. 1994, MNRAS, 266, 227
 Bardeen, J. M., Bond, J. R., Kaiser, N., & Szalay, A. S. 1986, ApJ, 304, 15
 Batjlik, S., Duncan, R., & Ostriker, J. P. 1988 ApJ, 327, 570
 Bechtold, J. 1994, ApJS, 91, 1
 Bi, H. G., Börner, G., & Chu, Y. 1992, A&A, 266, 1
 Bi, H. G., & Davidsen, A. F. 1997, ApJ, 479, 523
 Bi, H., Ge, J., & Fang, L.-Z. 1995, ApJ, 452, 90

Bond, J. R., Szalay, A. S. & Silk, J. 1988, ApJ, 324, 627

Cooke, A. J., Espey, B., & Carswell, B. 1997, MNRAS, 284, 552

Brainerd, T. G., Scherrer, R. J., & Villumsen, J. V. 1993, ApJ, 418, 570

Carswell, R. F., Lanzetta, K. M., Parnell, H. C., & Webb, J. K. 1991, ApJ, 371, 36

Carswell, R. F., Webb, J. K., Baldwin, J. A., & Atwood, B. 1987, ApJ, 319, 709

Cen, R., Miralda-Escudé, J., Ostriker, J. P. & Rauch, M. 1994, ApJ, 437, 9

Coles, P., Melott, A. L., & Shandarin, S. F. 1993, MNRAS, 260, 765

Cristiani, S., D'Odorico, S., Fontana, A., Giallongo, E., & Savaglio, S. 1995, MNRAS, 273, 1016

Davé, R., Hernquist, L., Weinberg, D. H., & Katz, N. 1997, ApJ, 477, 21

Doroshkevich, A. G. 1970, Astrofizika, 6, 581

Doroshkevich, A. G. & Shandarin, S. 1977, MNRAS, 179, 95

Giallongo, E., Cristiani, S., D'Odorico, S., Fontana, A., & Savaglio, S. 1996, ApJ, 466, 46

Gnedin, N. Y., & Hui, L. 1996, ApJ, 472, L73

Gnedin, N. Y., & Hui, L. 1997, in preparation

Gunn, J. E., & Peterson, B. A. 1965, ApJ, 142, 1633

Hernquist, L., Katz, N., Weinberg, D. H., & Miralda-Escudé, J. 1995, ApJ, 457, L51

Hockney, R. W., Eastwood, J. W. 1988, *Computer Simulation Using Particles*, Bristol: Adam Hilger

Hu, E., Kim, T., Cowie, L. L., Songaila, A., & Rauch, M. 1995, ApJ, 110, 1526

Hui, L., Bertschinger, E., 1996, ApJ, 471, 1

Hui, L., Gnedin, N. Y. 1996, preprint, astro-ph 9612232

Kauffmann, G., & Charlot, S. 1994, ApJ, 430, L97

Kofman, L., Pogosyan, D. Yu., & Shandarin, S. F. 1990, MNRAS, 242, 200

bibitem[Kofman 1991]kof91 Kofman, L. 1991, in *Primordial Nucleosynthesis and Evolution of Early Universe*, ed. K. Sato & J. Audouze (Dordrecht: Kluwer), 495

Kofman, L., Bertschinger, E., Gelb, J. M., Nusser, A., & Dekel, A. 1994, ApJ, 420, 44

Lu, L., Wolfe, A. M., & Turnshek, D. A., 1991, ApJ, 367, 19

Lu, L., Sargent, W. L. W., Womble, D. S., & Takada-Hidai, M. 1996, ApJ, 472, 590

Ma, C.-P. 1996, ApJ, 471, 13

Ma, C.-P., & Bertschinger, E. 1994, ApJ, 434, L5

Matarrese, S., Lucchin, F., Moscardini, L., & Saez, D. 1992, MNRAS, 259, 437

McGill, C. 1990, MNRAS, 242, 544

Meiksin, A., & Bouchet, F. R. 1995, ApJ, 448, L85

Melott, A. L. 1994, ApJ, 426, L19

Melott, A. L., Buchert, T., & Weiß, A. G. 1995, A&A, 294, 345

Miralda-Escudé, J., Cen, R., Ostriker, J. P., & Rauch, M. 1996, ApJ, 471, 582

Mo, H. J., & Miralda-Escudé, J. 1994, ApJ, 430, L25

Murdoch, H. S., Hunstead, R. W., Petinni, M., & Blades, J. C. 1986, ApJ, 309, 19

Pando, J., & Fang, L.-Z. 1996, ApJ, 459, 1

Peebles, P. J. E. 1980, *The Large Scale Structure of the Universe*, Princeton: Princeton University Press

Peebles, P. J. E. 1993, *Principles of Physical Cosmology*, Princeton: Princeton University Press

Petitjean, P., Mücket, J. P., & Kates, R. E. 1995, å, 295, L9

Petitjean, P., Webb, J. K., Rauch, M., & Carswell, R. F., & Lanzetta, K. 1993, MNRAS, 262, 499

Press, W. H., & Rybicki, G. B. 1993, ApJ, 418, 585

Press, W. H., Rybicki, G. B., Schneider, D. P. 1993, ApJ, 414, 64

Press, W. H., & Schechter, P. 1974, ApJ, 187, 425

Rees, M. 1986, MNRAS, 218, 25p

Reisenegger, A., & Miralda-Escudé, J. 1995, ApJ, 449, 476

Rugers, M., & Hogan, C. 1996, ApJ, 495, L1

Rybicki, G. B., Lightman, A. P. 1979, *Radiative Processes in Astrophysics*, New York: Wiley

Shandarin, S. F., & Zel'dovich, Y. 1989, Rev. Mod. Phys., 61, 185

Spitzer, L. 1978, *Physical Processes in the Interstellar Medium*, New York: Wiley

Tytler, D. 1987, ApJ, 321, 49

Tytler, D. 1992, In *Statistical Challenges in Modern Astronomy*, eds. Feigelson, E. D., & Babu, G. J., New York: Springer-Verlag

Tytler, D., & Burles, S. 1996, preprint, astro-ph 9606110

Weinberg, D. H., Hernquist, L., Katz, N., & Miralda-Escudé, J. 1996, In *Cold Gas at High Redshift*, eds. Bremer, M., Rottgering, H., Carilli, C., & van der Werf, P., Kluwer: Dordrecht

Zel'dovich, Ya. B. 1970, A&A, 5, 84

Zhang, Y., Anninos, P., & Norman, M. L. 1995, ApJ, 453, L57

Zhang, Y., Anninos, P., Norman, M. L., & Meiksin, A. 1996, preprint, astro-ph 9609194

Label	σ_8	n	k_S/Mpc^{-1}	Ω_b	σ_0	n_{eff}
CDM1a	0.7	1.0	2.3	0.05	1.12	–2
CDM1b	0.7	1.0	2.3	0.06	1.12	–2
CDM2	0.8	1.0	1.7	0.05	1.13	–1.94
CDM3	0.57	1.0	1.7	0.05	0.81	–1.94
CDM4	0.46	1.0	4.9	0.05	1.01	–2.17
CDM5	0.8	0.5	8.4	0.05	1.01	–2.59

Table 1: A list of all the CDM models discussed in this paper. All have $h = 0.5$. The larger scale power-spectral index is n . Every model has $\Omega_b = 0.05$ except for CDM1b, which has a higher baryon content and is shown in Fig. 5. The truncation scales k_S for CDM1a, CDM1b and CDM2 are defined by $k_S = 1.5 k_{\text{NL}}$ (eq. [15]). The smoothing scales for the rest of the models are chosen for the purpose of testing (see Sec. 7) but always larger than the length scale defined above. The rms density fluctuation σ_0 and the small scale effective slope of the power spectrum n_{eff} are defined in equations (37) and (39), for the value of k_S given here. We assume $\bar{z} = 3$. The rms linear density fluctuation in a sphere of radius $8h^{-1} \text{ Mpc}$ is equal to σ_8 .

Label	Ω_ν	h	n	$Q_{\text{rms}}/\mu\text{K}$	T/S	k_S/Mpc^{-1}	σ_8	σ_0	n_{eff}
A1	0.1	0.5	0.95	18.5	$7(1-n)$	3.8	0.73	1.08	-2.23
A2	0.2	0.5	0.95	18.5	$7(1-n)$	8.4	0.66	0.84	-2.48
A3	0.3	0.5	0.95	18.5	$7(1-n)$	not apply	0.64	not apply	not apply
B1	0.1	0.5	0.9	19.2	0	3.3	0.82	1.08	-2.25
B2	0.2	0.5	0.9	19.2	0	8.4	0.73	0.87	-2.52
C1	0.1	0.65	0.9	19.2	$7(1-n)$	3.1	0.82	1.09	-2.14
C2	0.2	0.65	0.9	19.2	$7(1-n)$	10.9	0.76	1.02	-2.5
D1	0.1	0.65	0.8	20.5	0	2.8	0.94	1.08	-2.19
D2	0.2	0.65	0.8	20.5	0	10.9	0.87	1.02	-2.57

Table 2: A list of all the CHDM models discussed in this paper. All have $\Omega_b = 0.05$. The parameters are defined as follows: Ω_ν is the density parameter in neutrino, n is the large scale spectral index of the power spectrum, Q_{rms} is the COBE quadrupole in μK and T/S is the tensor to scalar ratio. The smoothing wavenumber k_S for each $\Omega_\nu = 0.1$ model is $1.5 k_{\text{NL}}$ (eq. [15]) and k_S for each $\Omega_\nu = 0.2$ model is the Jeans scale for $\gamma = 1.5$, $T_0 = 10^4 K$ and the corresponding h (see Sec. 3.2). No simulation is run for A3, so no k_S is listed. The rms linear density fluctuation σ_0 and the small scale effective spectral slope n_{eff} are defined in equations (37) and (39), for each value of k_S given in the seventh column. The models and their power spectra are taken from Ma (1996).

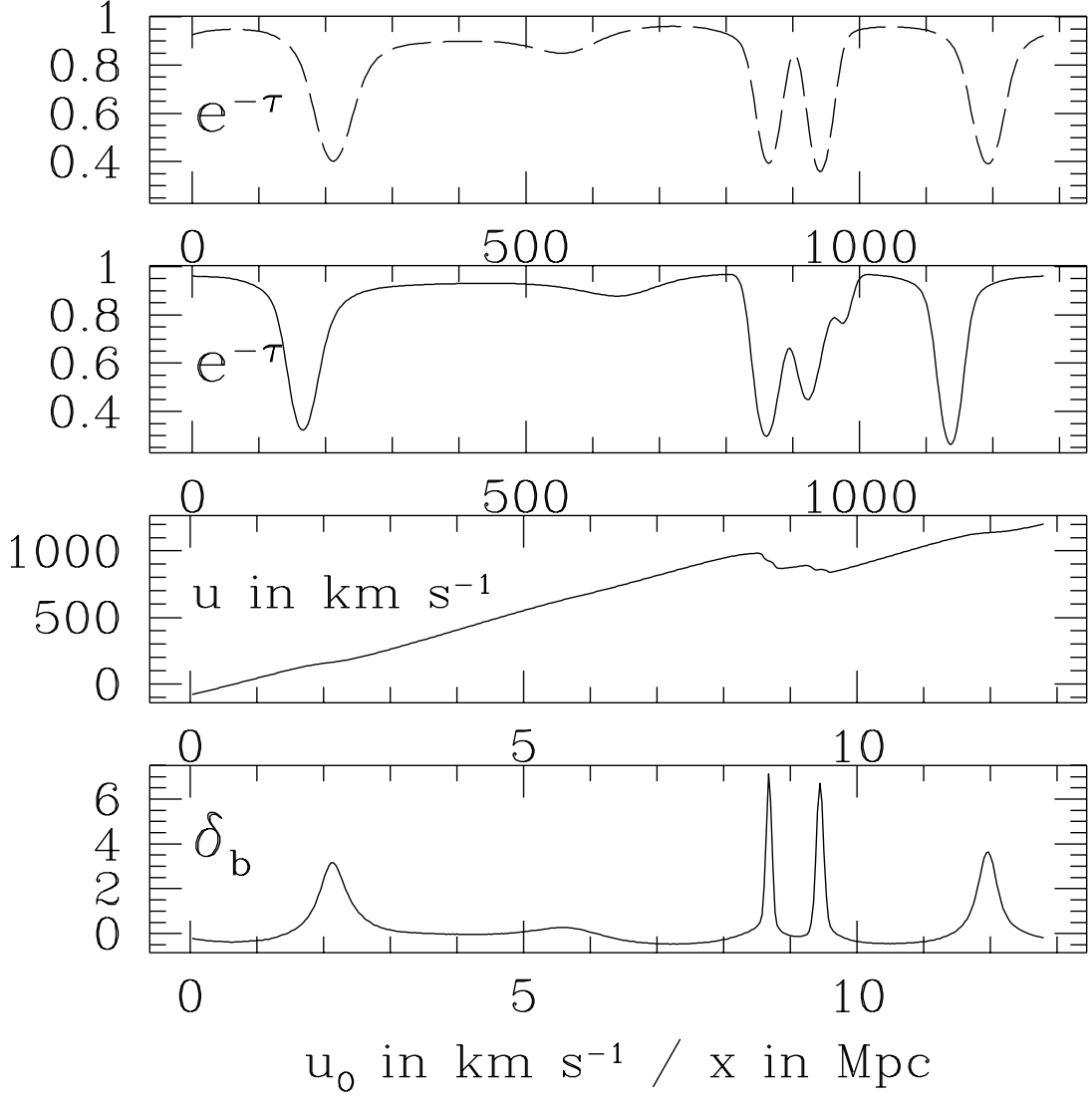


Fig. 1.— A line of sight through a $\sigma_8 = 0.7$ CDM simulation (produced using the truncated Zel'dovich approximation) at $\bar{z} = 3$, with $h = 0.5$. The transfer function is taken from Ma (1996). Box size is 12.8 Mpc with a grid spacing of 0.032 Mpc. The parameters are $\Omega_b h^2 = 0.0125$, $J_{\text{HI}} = 0.5$, $T_0 = 10^4 \text{ K}$, $\gamma = 1.5$ and $k_S = 2.3 \text{ Mpc}^{-1}$. All distances are comoving. See Sec. 3 for definitions of the symbols. The abscissas for the lower two panels are the comoving distances along the line of sight in units of Mpc. The lower of the two panels is the profile of overdensity δ_b (eq. [8]) and the upper one is the profile of velocity u (eq. [3]). The top two panels are both transmission profiles where τ is the Ly α optical depth and the abscissas represent u_0 , which is related to the observed frequency through equation (4). The profile with solid line is obtained using the full density and peculiar velocity fields. The profile with dashed line is obtained using the same density field but setting the peculiar velocity to zero everywhere (in which case, u becomes linear in x).

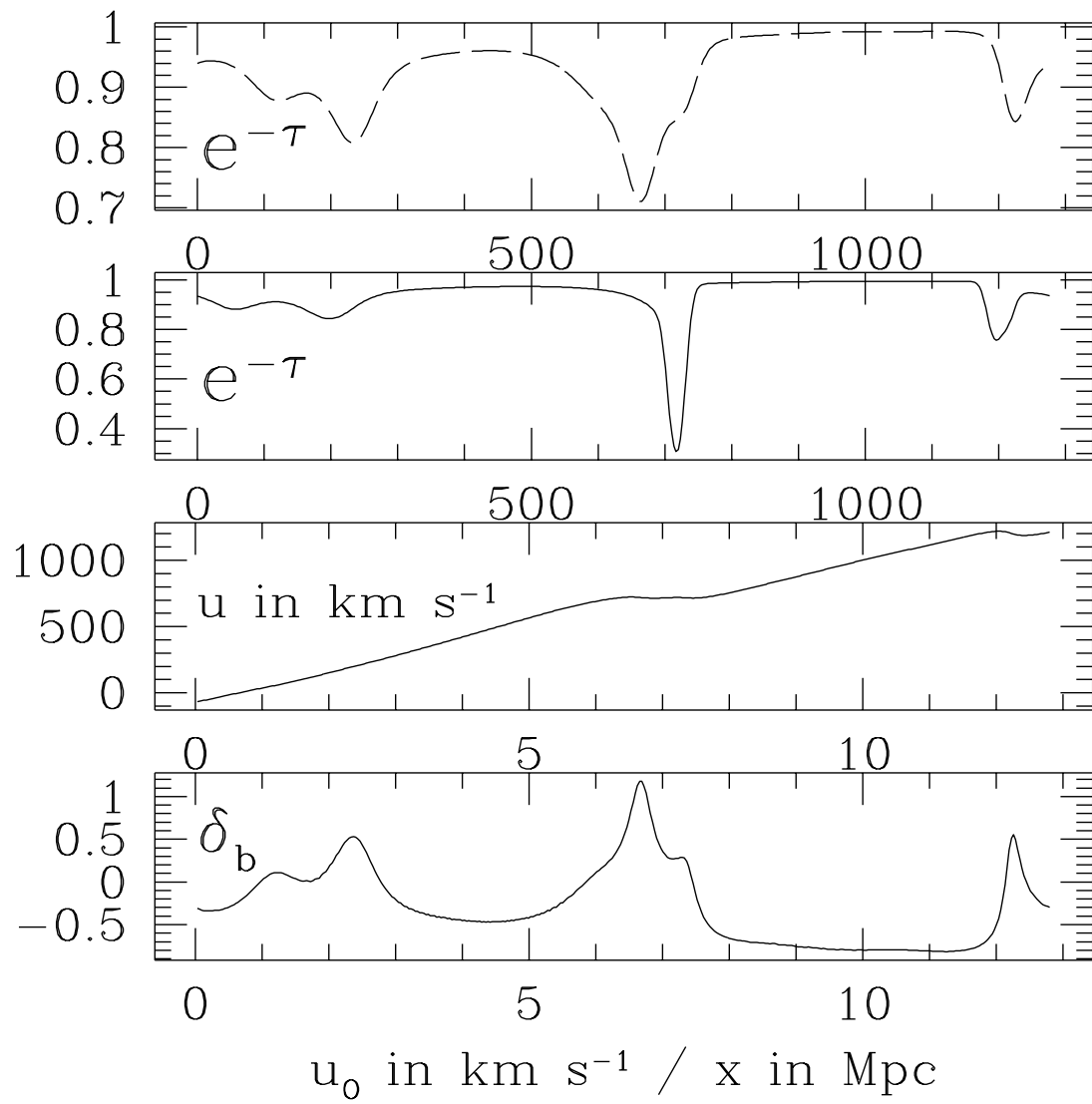


Fig. 2.— The same as in Fig. 1 but a different line of sight.

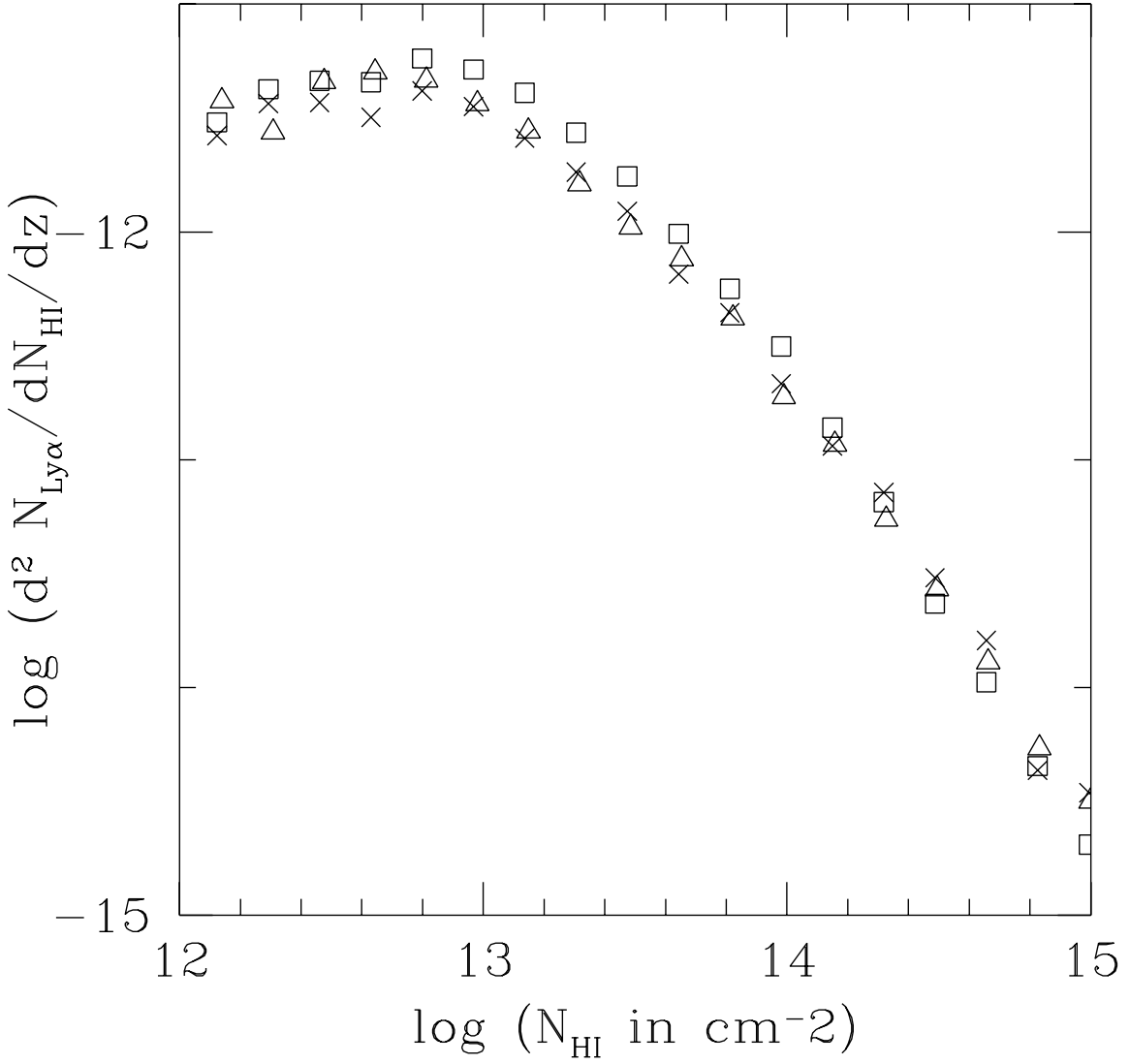


Fig. 3.— The column density distributions for the same model and parameters as those in Fig. 1. The quantity $d^2 N_{\text{Ly}\alpha} / dN_{\text{HI}} / dz$ has units of cm^2 . Crosses represent the distribution obtained by applying the Threshold-Algorithm (threshold at 0.89, which is the mean transmission) to spectra generated using the density and peculiar velocity fields predicted by the truncated Zel'dovich approximation. Open triangles represent the same except that peculiar velocities are set to zero. Open squares are obtained by applying the Threshold-Deblending-Algorithm at the threshold of 0.89.

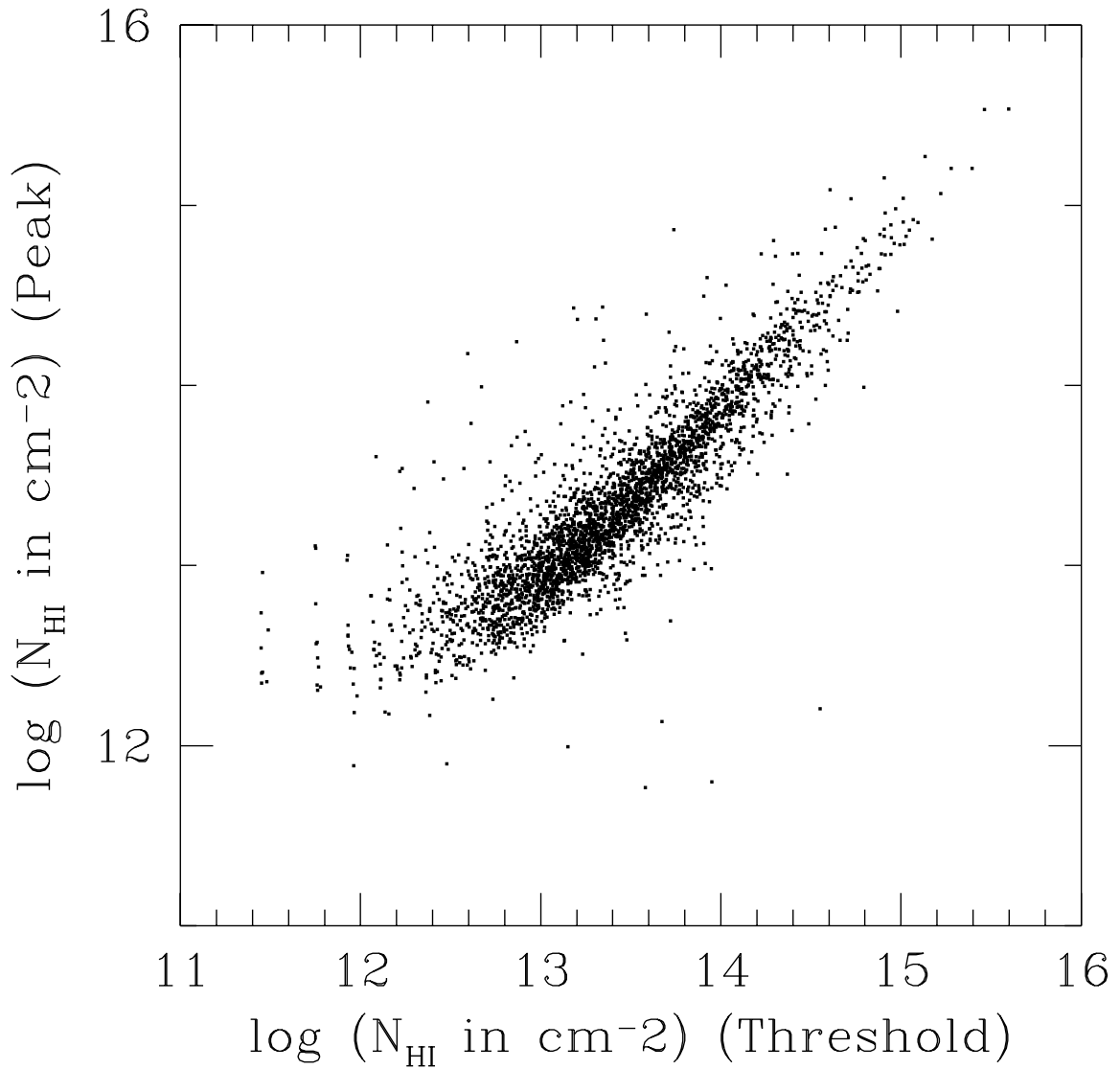


Fig. 4.— Same parameters as in Fig. 1. The column densities computed using two different methods are plotted against each other. First, we identify absorption lines by the Threshold-Deblending-Algorithm using a transmission threshold of 0.89 and assign column densities according to equation (21), which are plotted as the abscissas. We then take each absorption line identified using the Threshold-Deblending-Algorithm and search for the corresponding maximum in δ_b and apply equation (27) to assign a second set of column densities, which are plotted as the ordinates.

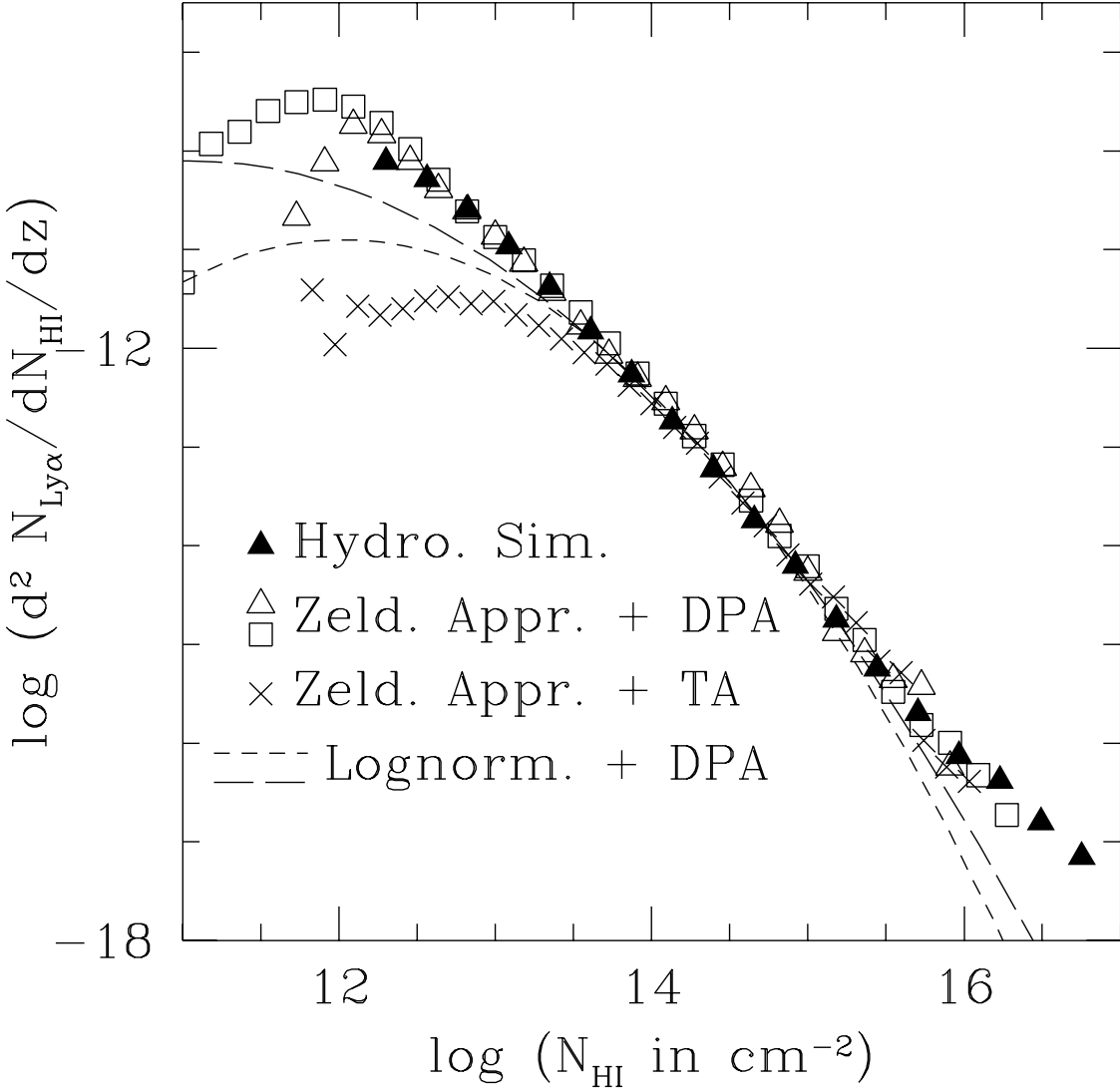


Fig. 5.— The model CDM1b (Table 1) at $\bar{z} = 3$, $J_{\text{HI}} = 0.325$, $T_0 = 10^4 K$ and $\gamma = 1.45$. Solid triangles represent the distribution obtained by applying the Voigt-profile-fitting-technique to synthetic spectra from a full hydrodynamic simulation (Zhang et al. 1996) with box size of 9.6 Mpc comoving and grid spacing of 0.075 Mpc. Open triangles and open squares are the predictions of the Density-Peak-Ansatz (DPA) coupled with the truncated ($k_S = 2.3 \text{ Mpc}^{-1}$) Zel'dovich approximation, the former using the same box size and grid-spacing as the hydrodynamic simulation and the latter using a box size of 12.8 Mpc and grid spacing of 0.05 Mpc. Crosses are the results of applying the Density-Peak-Ansatz and the Threshold-Algorithm (TA; transmission threshold at 0.83, the mean transmission) to the same density field as for the open squares. The short-dashed and long-dashed curves are the predictions of the Density-Peak-Ansatz coupled with the lognormal approximation, the former with $k_S = 2.3 \text{ Mpc}^{-1}$ and the latter with the smoothing scale chosen so that the final rms density fluctuation matches that of the Zel'dovich approximation ($k_S = 3.6 \text{ Mpc}^{-1}$).

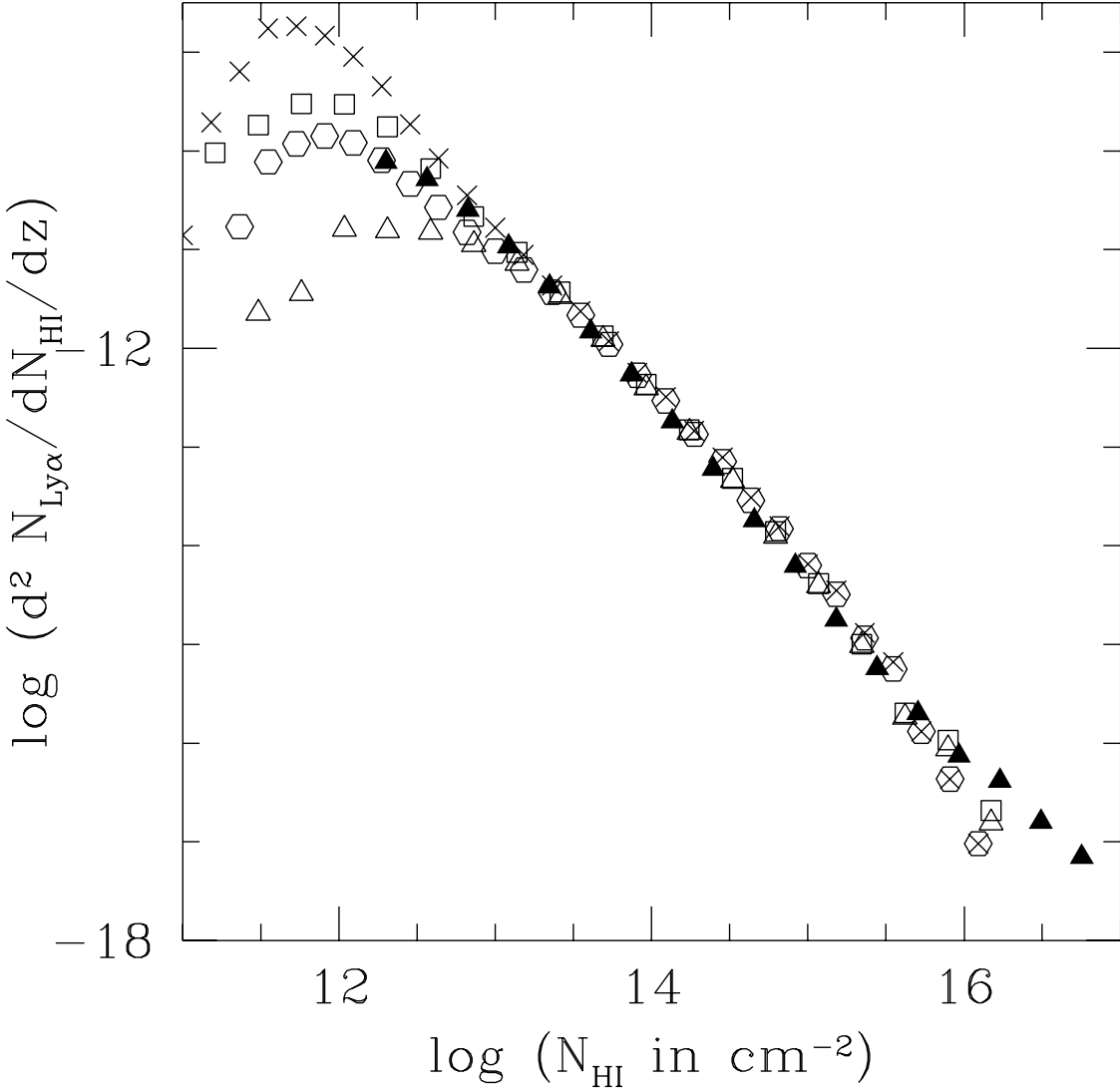


Fig. 6.— The solid triangles are same as those in Fig. 5, representing the column density distribution obtained by applying the Voigt-profile-fitting-technique to synthetic spectra from a full hydrodynamic simulation. The rest of the points represent the column density distributions obtained using the Density-Peak-Anätz in conjunction with the truncated Zel'dovich approximation for two simulations of different resolutions but the same cosmological, thermal and ionization parameters as in Fig. 5. The open squares and open triangles represent the distributions of a simulation with box size of 12.8 Mpc and grid spacing of 0.05 Mpc (all distances quoted are comoving). The open squares here are the same as those in Fig. 5 where each maximum over three cells is identified as a peak. The open triangles are the result of a different definition of peaks: a local maximum over five cells with the density slope on each side of the maximum not changing signs. Similarly, the crosses and open hexagons are the distributions for a simulation of box size 12.8 Mpc and grid spacing 0.0284 Mpc, using the three-cell and five-cell definition of peaks respectively.

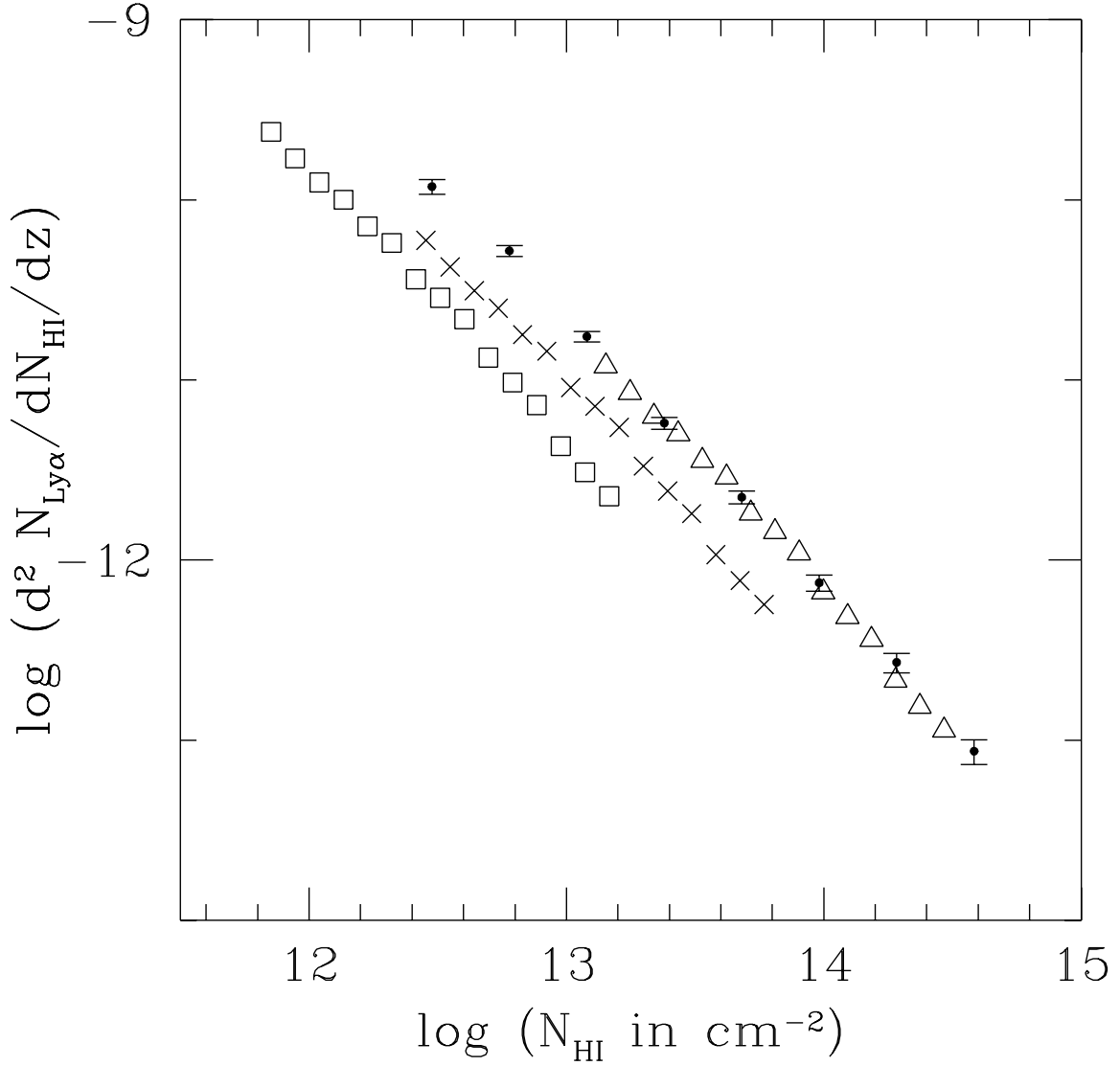


Fig. 7.— The column density distribution of the $\sigma_8 = 0.7$ CDM model with no tilt (CDM1a in Table 1), obtained using the Density-Peak-Ansatz and the truncated Zel'dovich approximation ($k_S = 2.3 \text{ Mpc}^{-1}$). The redshift is $\bar{z} = 3$. Box size is 12.8 Mpc with grid spacing of 0.05 Mpc. Open squares: $F = 0.25$ (eq. [32]). Crosses: $F = 1$. Open triangles: $F = 5$. All of them have the equation of state described by $\gamma = 1.5$ (eq. [19]). The points with error bars are the observational data at about $\bar{z} = 3$ which have been corrected for incompleteness, taken from Hu et al. (1995).

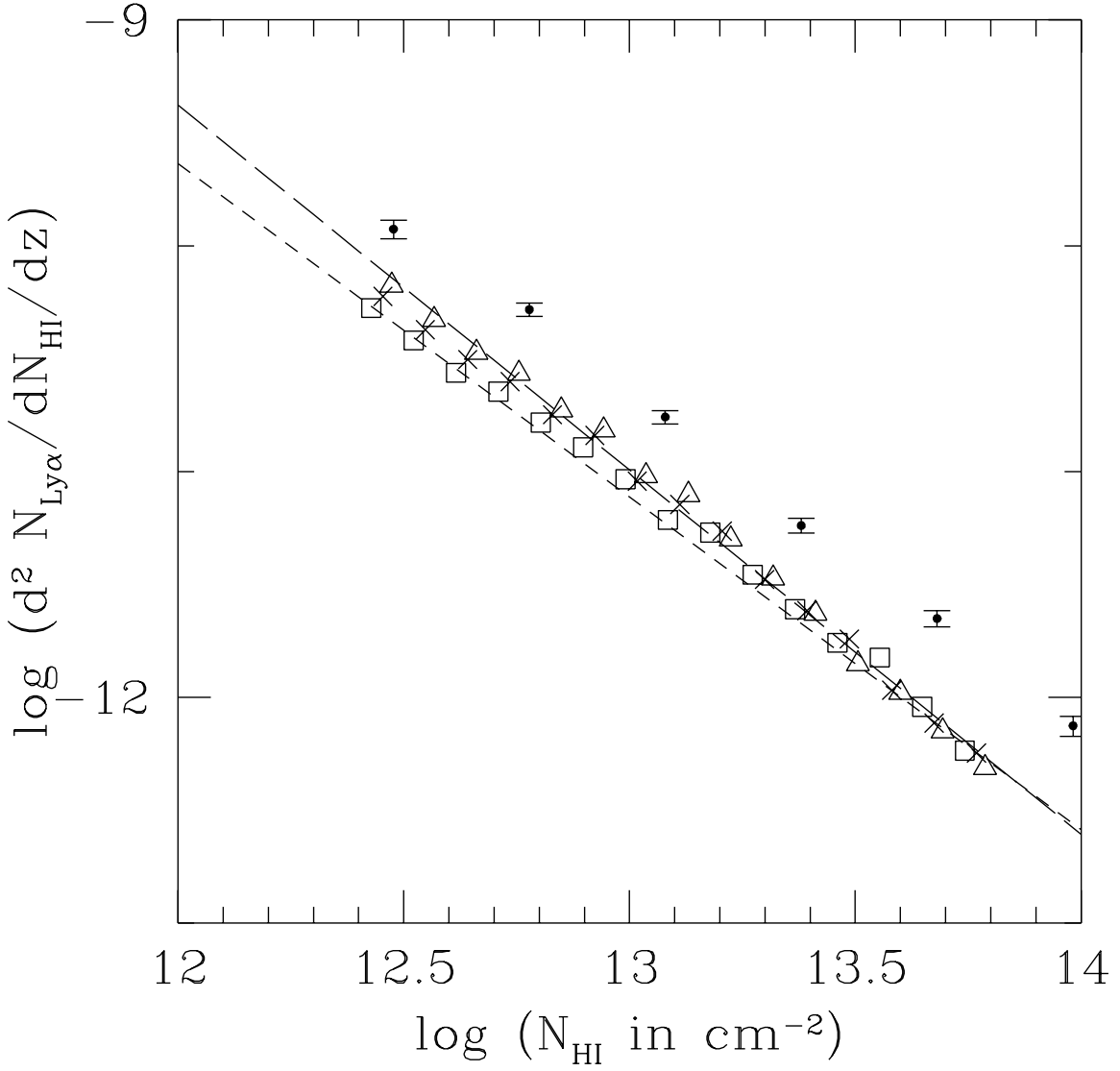


Fig. 8.— Column density distributions of the CDM1a model (Table 1) for three different equations of state (eq. [19]). Open squares: $\gamma = 1.2$; crosses (same as crosses in Fig. 7): $\gamma = 1.5$; open triangles: $\gamma = 1.7$. $F = 1$ (defined in eq. [32]) for all three. Points with error-bars are the same observational data as in Fig. 7. Long-dashed and short-dashed lines have the approximate slopes ($\beta = 1.62$ and $\beta = 1.48$) (normalization is chosen by hand) as given in equation (41) for the open triangles and open squares respectively.

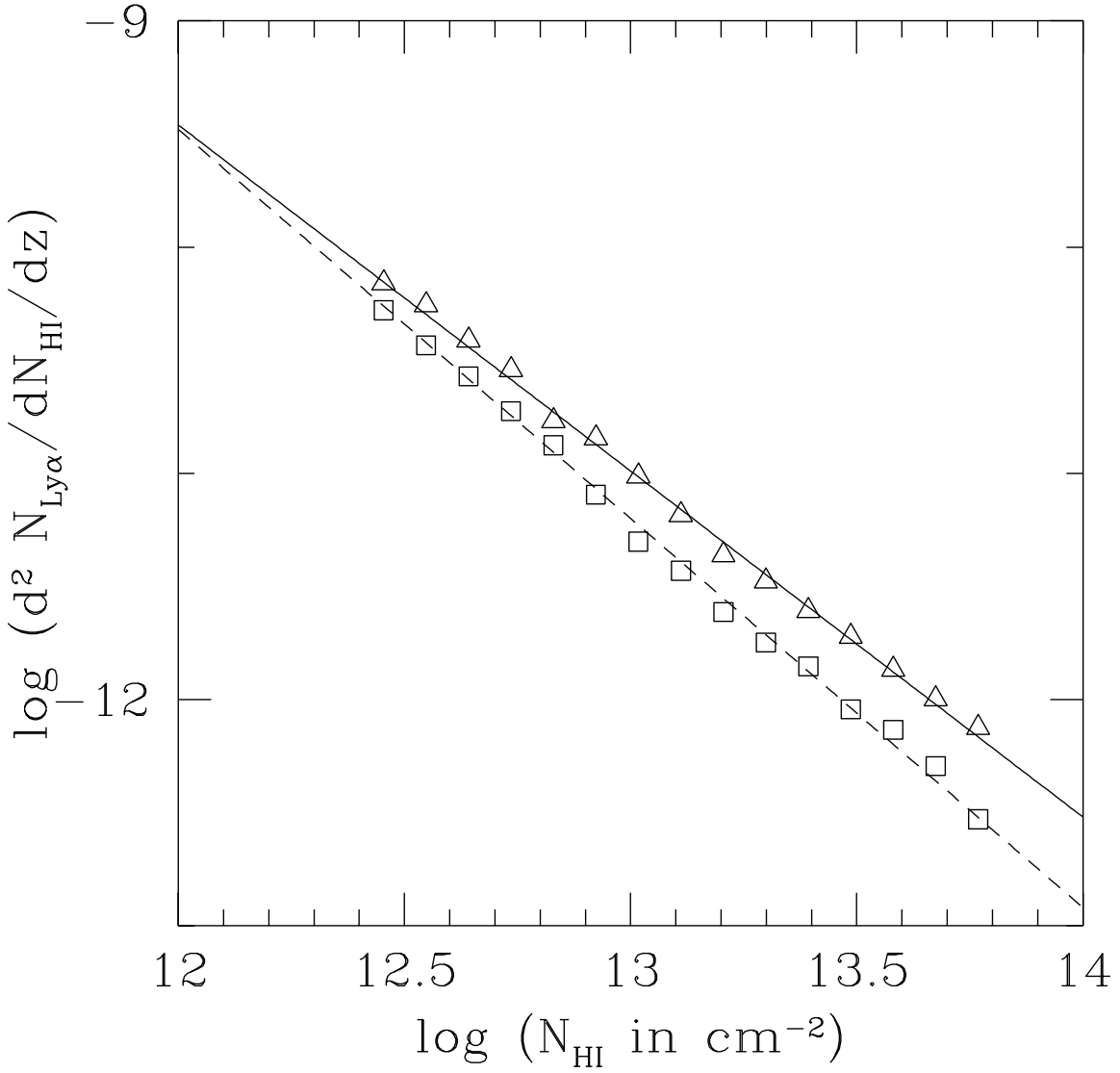


Fig. 9.— The effect of the amplitude of power spectrum on the slope of the column density distribution. Open triangles represent the CDM2 model with $\sigma_0 = 1.13$ and $n_{\text{eff}} = -1.94$ and open squares represent the CDM3 model with $\sigma_0 = 0.81$ and the same n_{eff} (see Table 1). The normalizations of the column density distributions are chosen by hand. The solid and dashed lines have the approximate slopes ($\beta = 1.53$ and $\beta = 1.72$) as given in equation (41) for the open triangles and squares respectively.

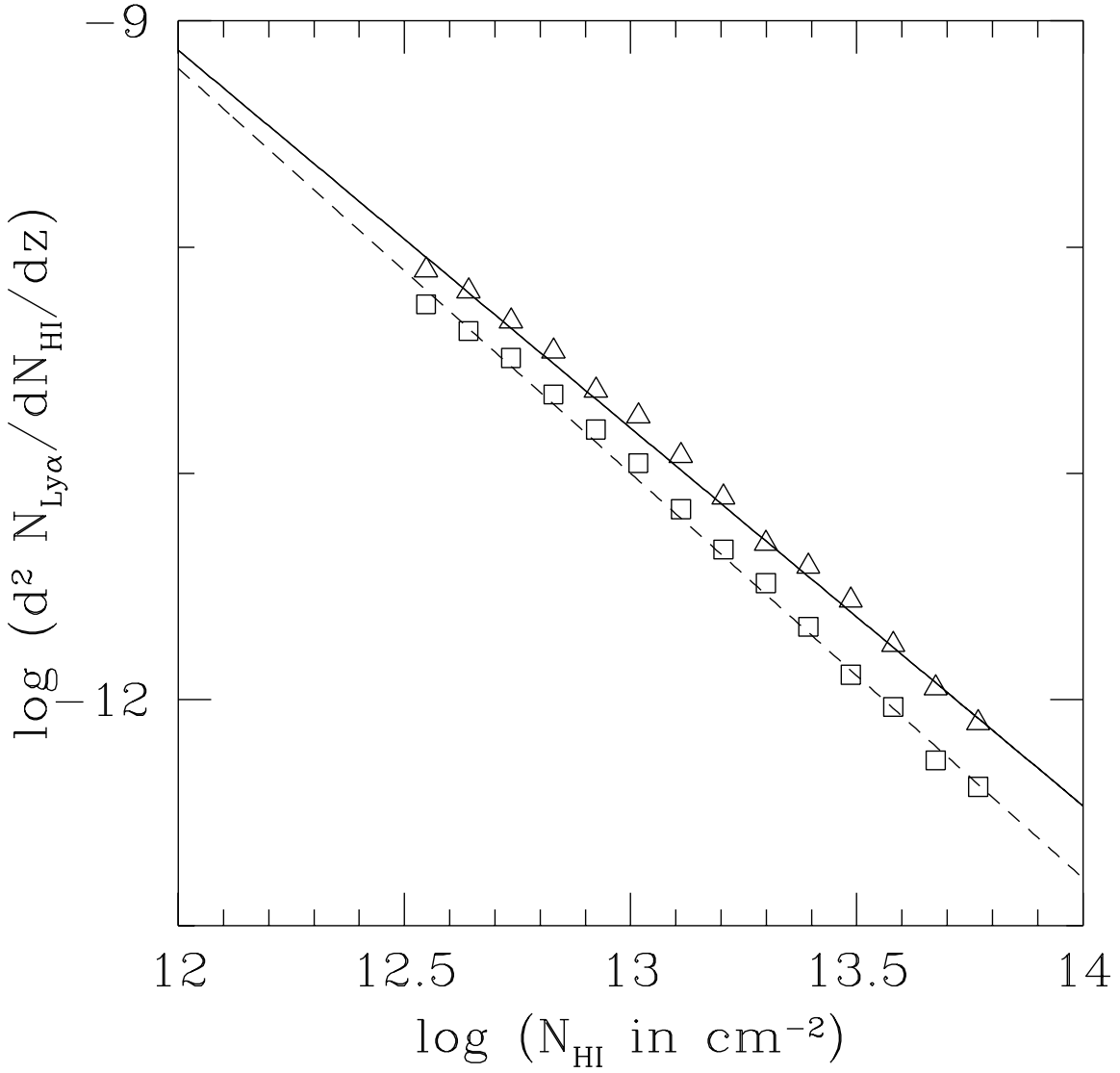


Fig. 10.— The effect of the shape of the power spectrum on the slope of the column density distribution. Open triangles represent the CDM4 model with $\sigma_0 = 1.01$ and $n_{\text{eff}} = -2.17$ and open squares represent the CDM5 model with the same σ_0 and $n_{\text{eff}} = -2.59$ (see Table 1). The normalizations of the column density distributions are chosen by hand. The solid and dashed lines have the approximate slopes ($\beta = 1.67$ and $\beta = 1.79$) as given in equation (41) for the open triangles and squares respectively.

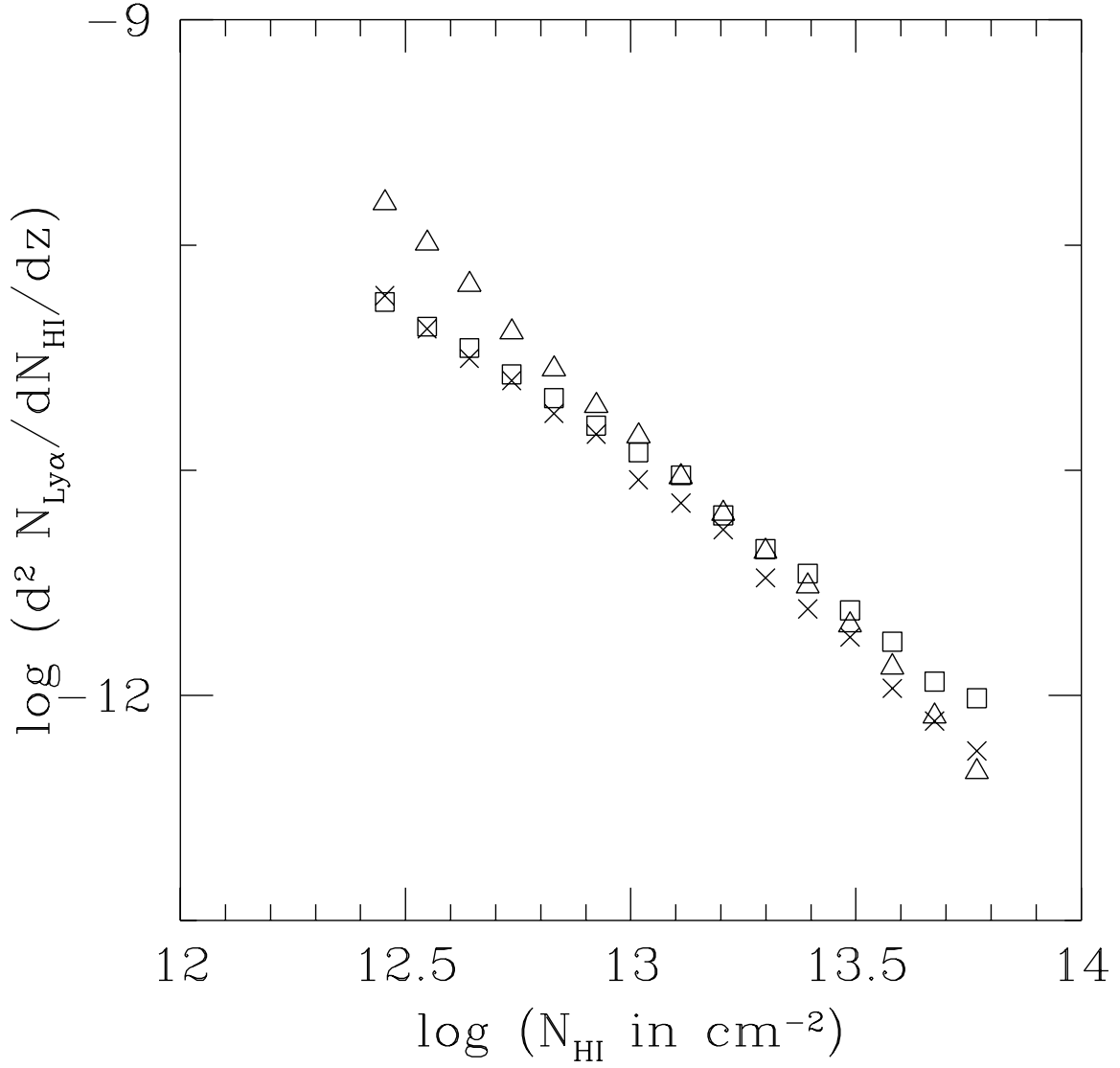


Fig. 11.— Column density distributions of the CDM1a model (Table 1) for three different initial smoothing scales. Crosses (same as crosses in Fig. 7): $k_S = 2.3 \text{ Mpc}^{-1}$, which is the smoothing scale according to the standard prescription (eq. [15]). Open triangles: $k_S = 1.15 \text{ Mpc}^{-1}$. Open squares: $k_S = 8.4 \text{ Mpc}^{-1}$, which is the Jeans scale for $T_0 = 1$ and $\gamma = 1.5$. Significant amount of orbit-crossing has probably taken place for the last case. We adopt $F = 1$ (eq. [32]) and $\gamma = 1.5$ (eq. [19]) for all three cases.

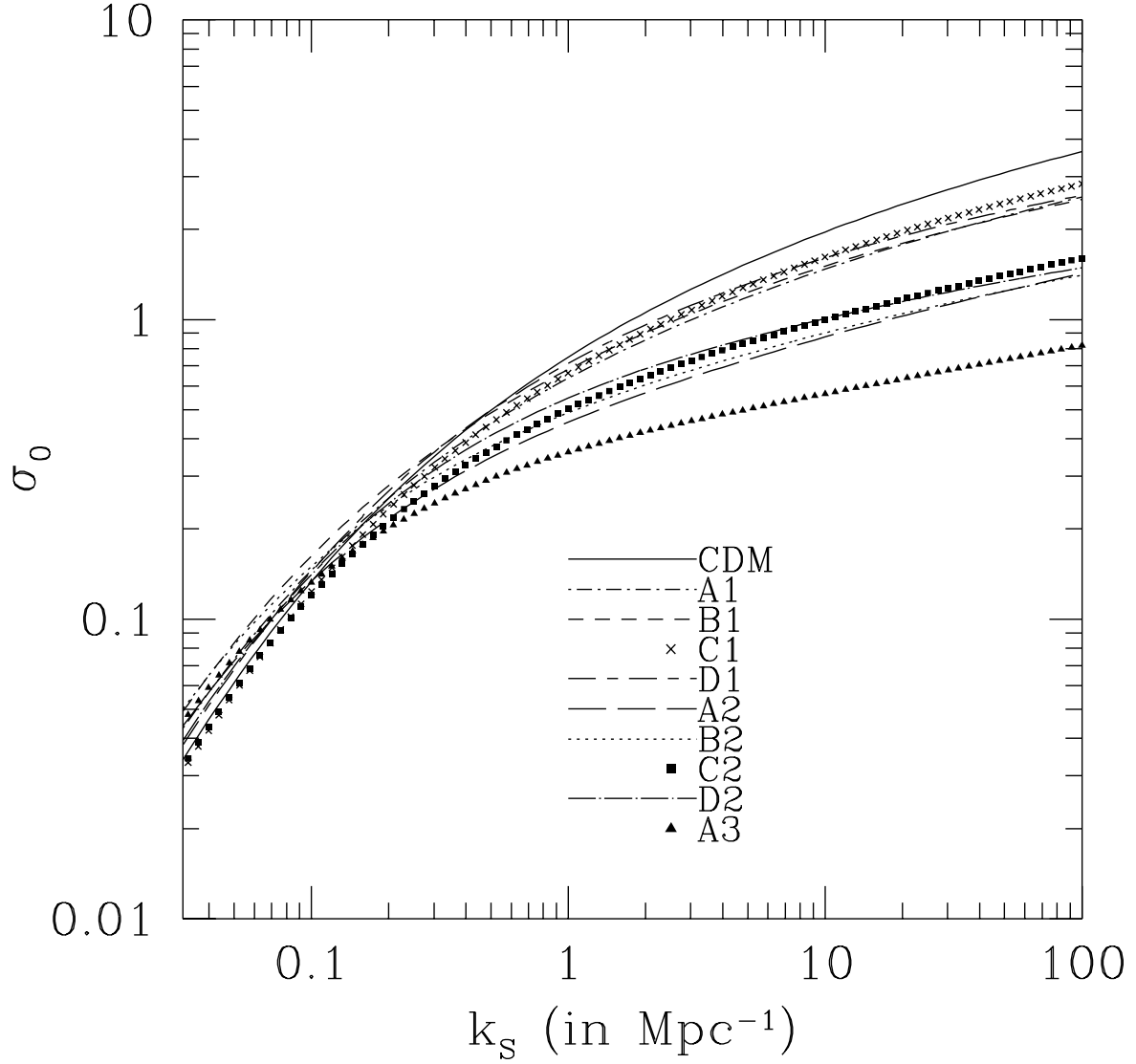


Fig. 12.— σ_0 versus k_S (eq. [37]) at $\bar{z} = 3$. Going from the top, the solid line is the same $\sigma_8 = 0.7$, $h = 0.5$ CDM model with no tilt as in Fig. 7; the next four sets of points/lines close together are all $\Omega_\nu = 0.1$ CHDM models, A1, B1, C1 and D1 in Table 2 ; the next four sets are all $\Omega_\nu = 0.2$ CHDM models, A2, B2, C2 and D2; the last set, solid triangles, is an $\Omega_\nu = 0.3$ CHDM model, A3. Note that $\sigma_0(k_S) \propto k_S^{(n_{\text{eff}}+3)/2}$ (see eq. [39]).

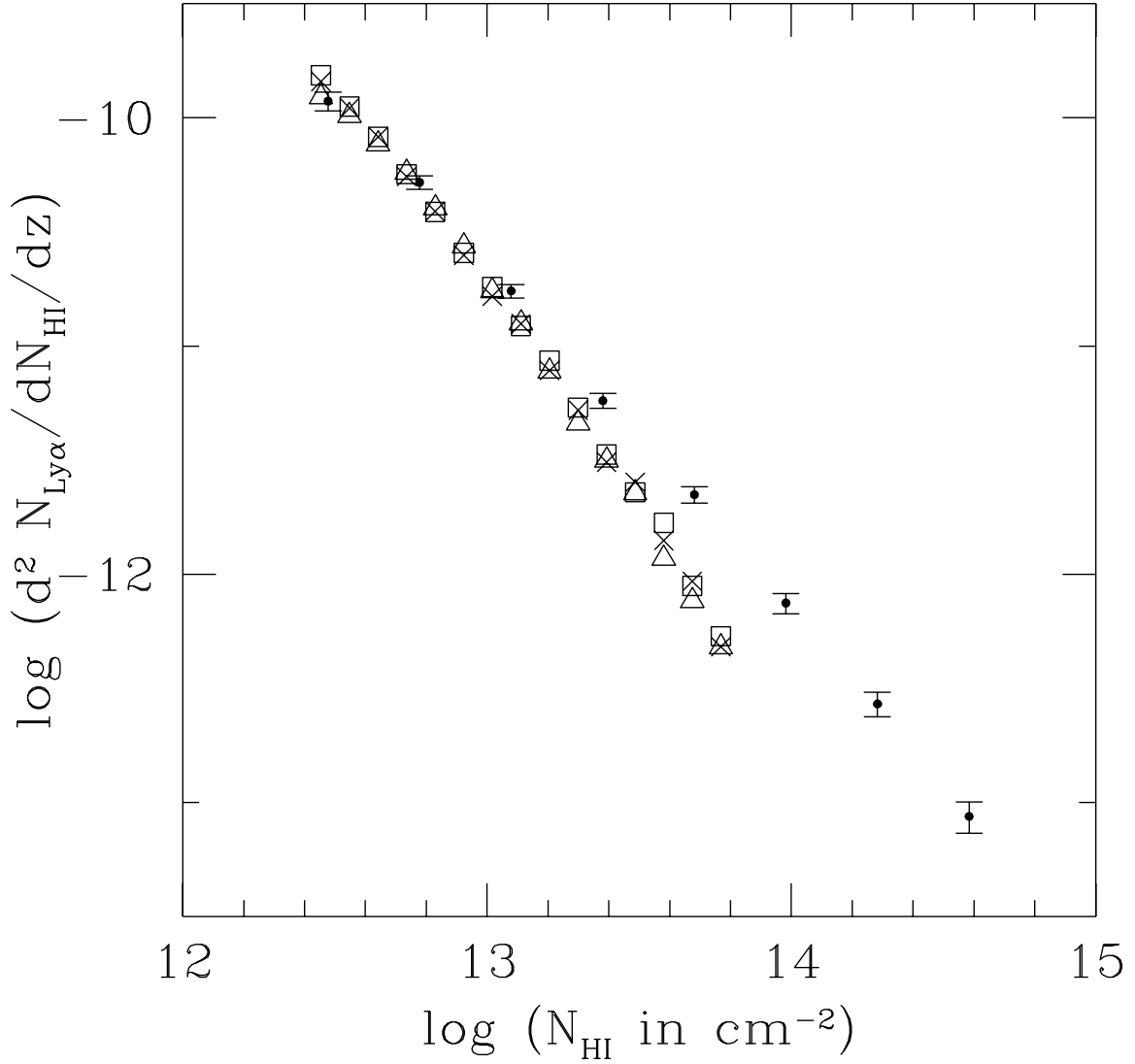


Fig. 13.— Column density distributions of the B2 CHDM model (see Table 2) for three initial smoothing scales. Crosses: $k_S = 19.2 \text{ Mpc}^{-1}$ (standard truncation prescription, $k_S = 1.5 k_{\text{NL}}$ according to eq. [15]). Open triangles: $k_S = 8.4 \text{ Mpc}^{-1}$ (Jeans scale for $T_0 = 10^4$ and $\gamma = 1.5$). Open squares: no smoothing at all. Points with error-bars are the observational data as in Fig. 7. For all models, $F = 1$ (eq. [32]) and $\gamma = 1.5$ (eq. [19]) are used.

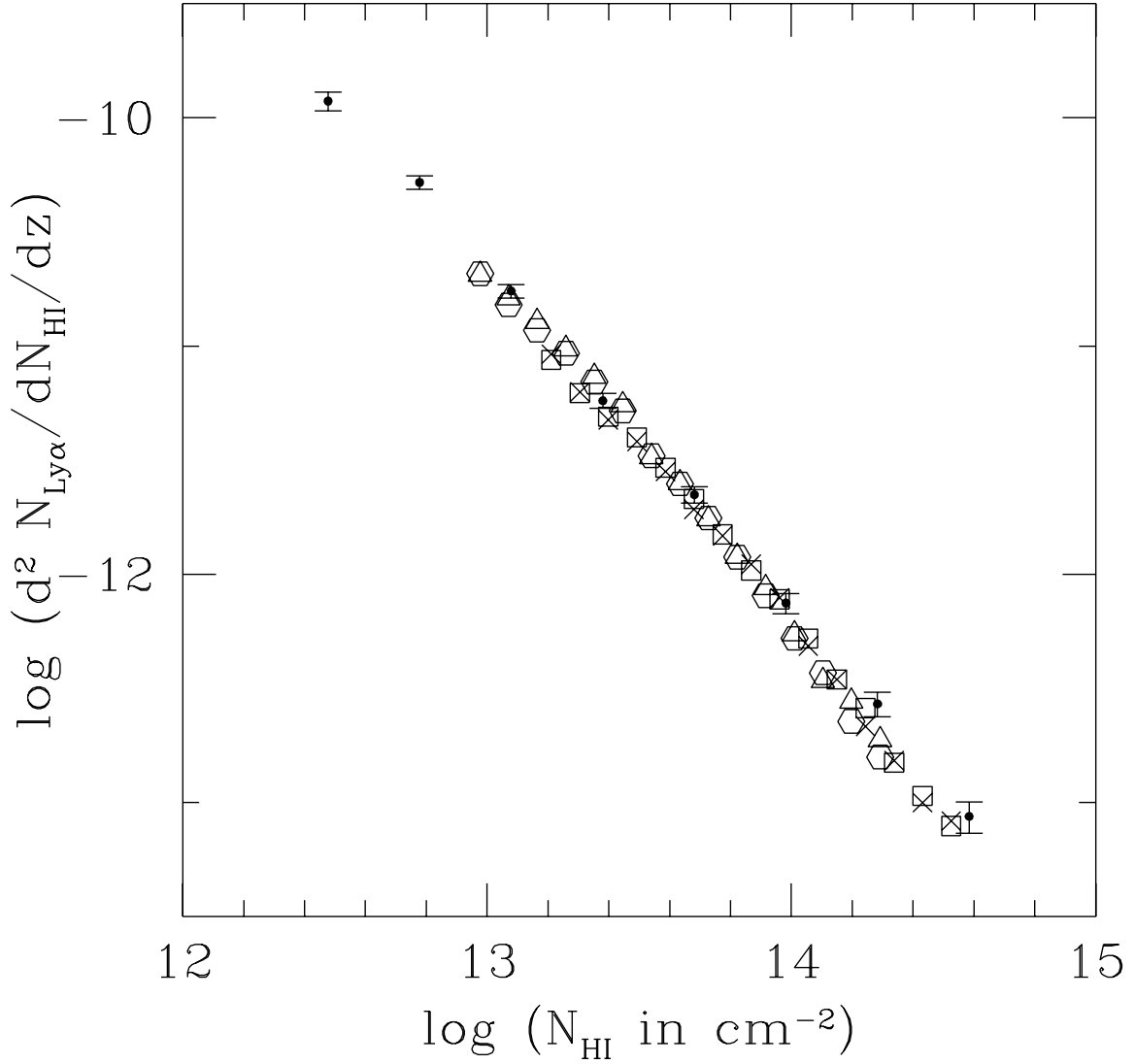


Fig. 14.— Column density distributions for four $\Omega_\nu = 0.1$ CHDM models. Points with error-bars are the observational data as in Fig. 7. All models have $\Omega_\nu = 0.1$. We use $\gamma = 1.5$ in the equation of state for all of them (eq. [19]). Table 2 contains descriptions of each of the following models. Open hexagons: B1, $F = 3.33$. Open triangles: A1, $F = 3.33$. Crosses: D1, $F = 5.7$. Open squares: C1, $F = 5.7$. F is defined in equation (32).

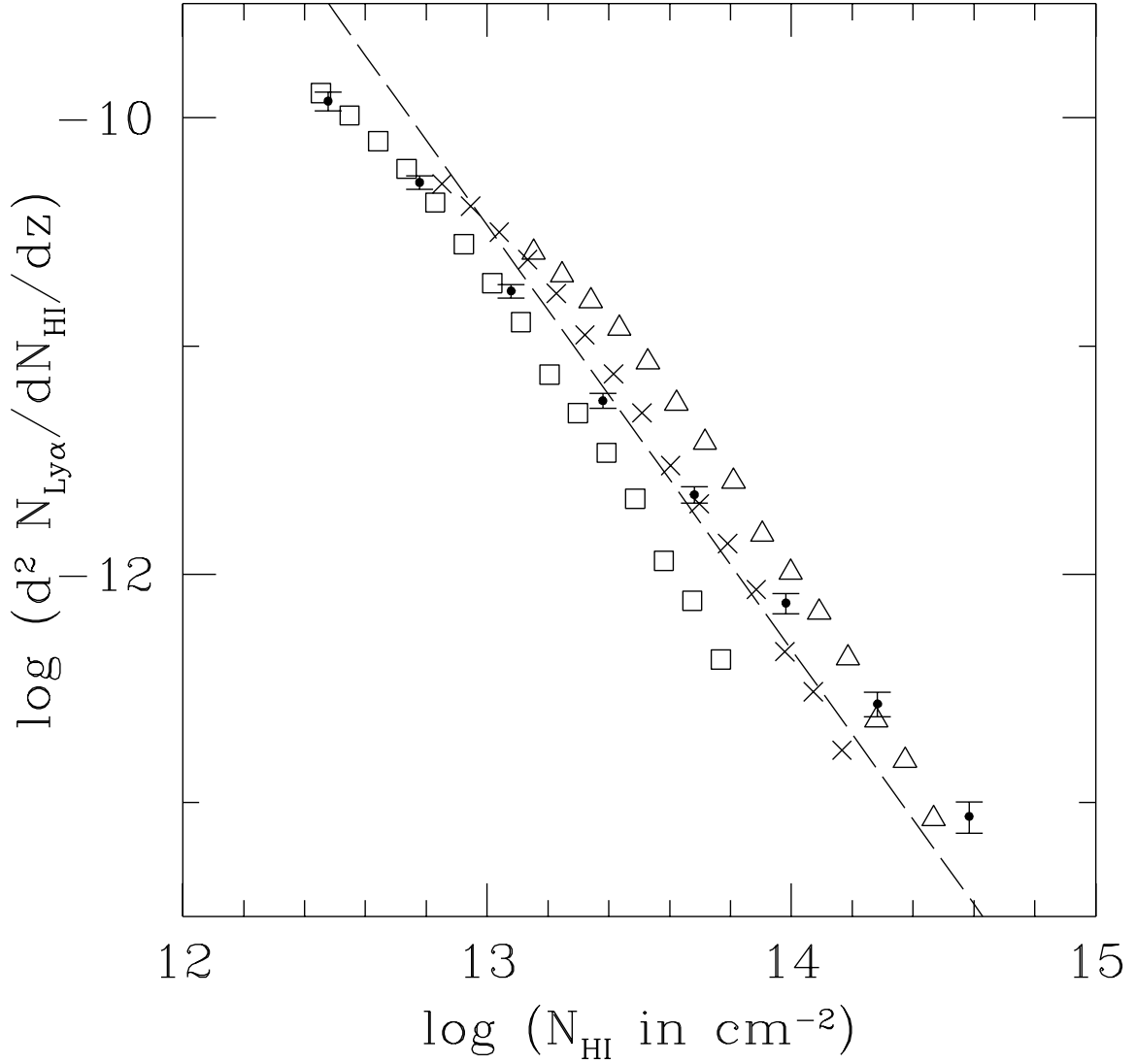


Fig. 15.— The column density distribution for the *A2* CHDM model (Table 2). Three values of F (eq. [32]) are shown: $F = 1$ (open squares), $F = 2.5$ (crosses) and $F = 5$ (open triangles). We choose $\gamma = 1.5$ for all three (eq. [19]). Points with error-bars are the observational data as in Fig. 7. The dashed line has the slope of $\beta = 1.86$, as given in equation (41). The normalization of the line is chosen by hand.

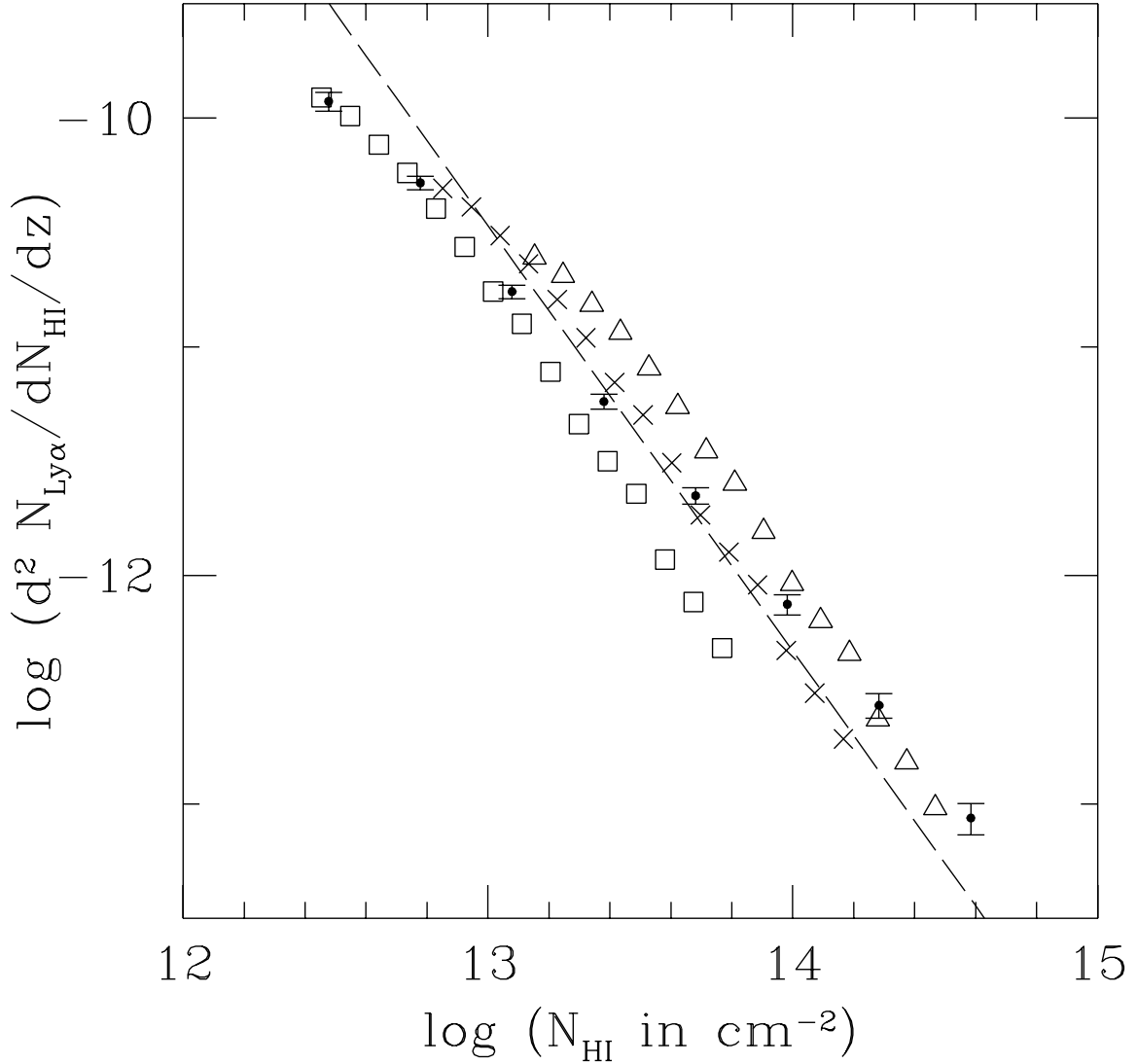


Fig. 16.— The column density distribution for the *B2* CHDM model (Table 2). Three values of F are shown (eq. [32]): $F = 1$ (open squares), $F = 2.5$ (crosses) and $F = 5$ (open triangles). $\gamma = 1.5$ for all three (eq. [19]). Points with error-bars are the observational data as in Fig. 7. The dashed line has a slope of $\beta = 1.86$, as given in equation (41).

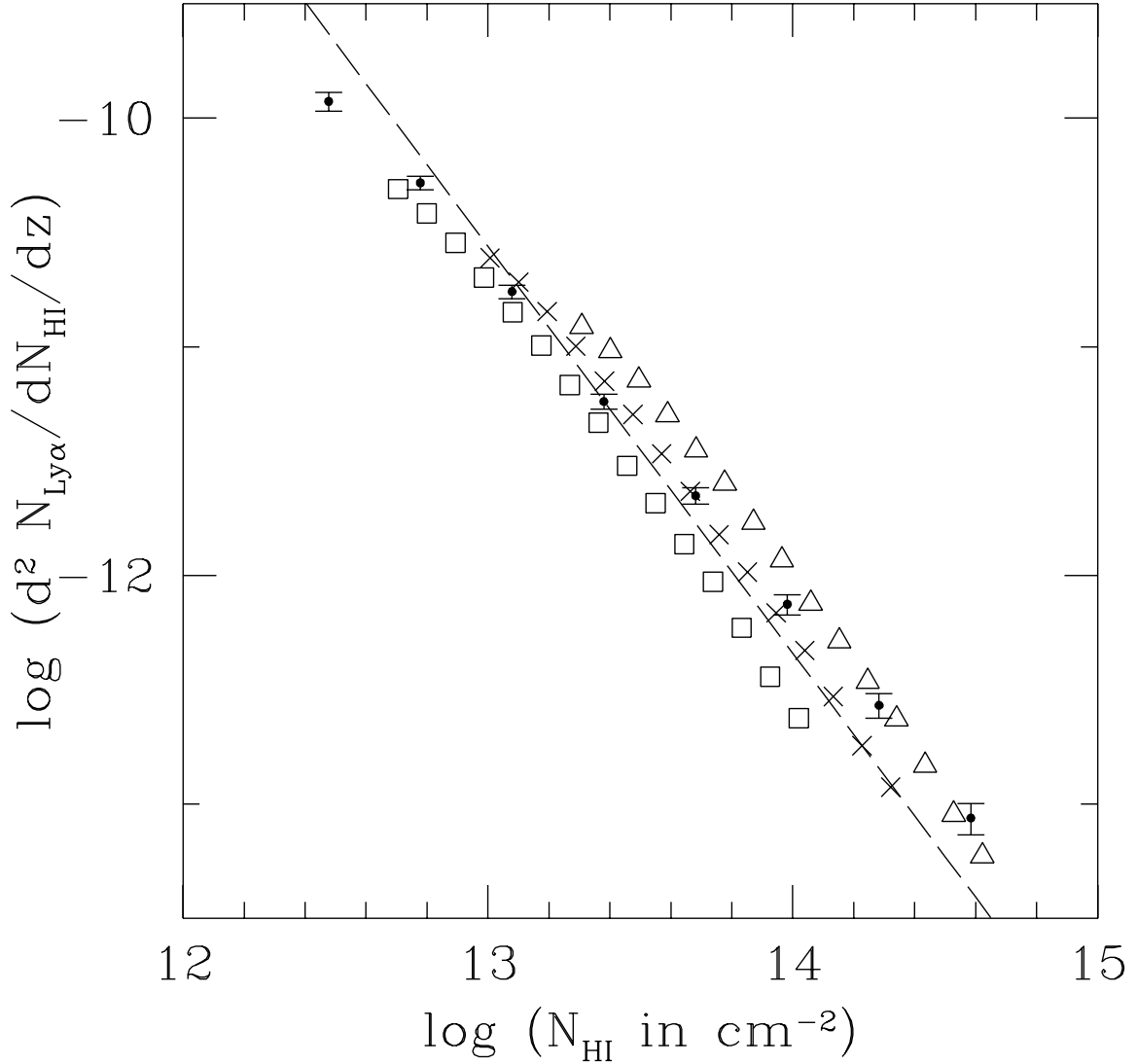


Fig. 17.— The column density distribution for the $D2$ (Table 2) CHDM model. Three values of F are shown (eq. [32]): $F = 7.14$ (open triangles), $F = 3.57$ (crosses) and $F = 1.79$ (open squares). $\gamma = 1.5$ for all three (eq. [19]). Points with error-bars are the same observational data as in Fig. 7. The dashed line has a slope of $\beta = 1.78$, as given in equation (41).

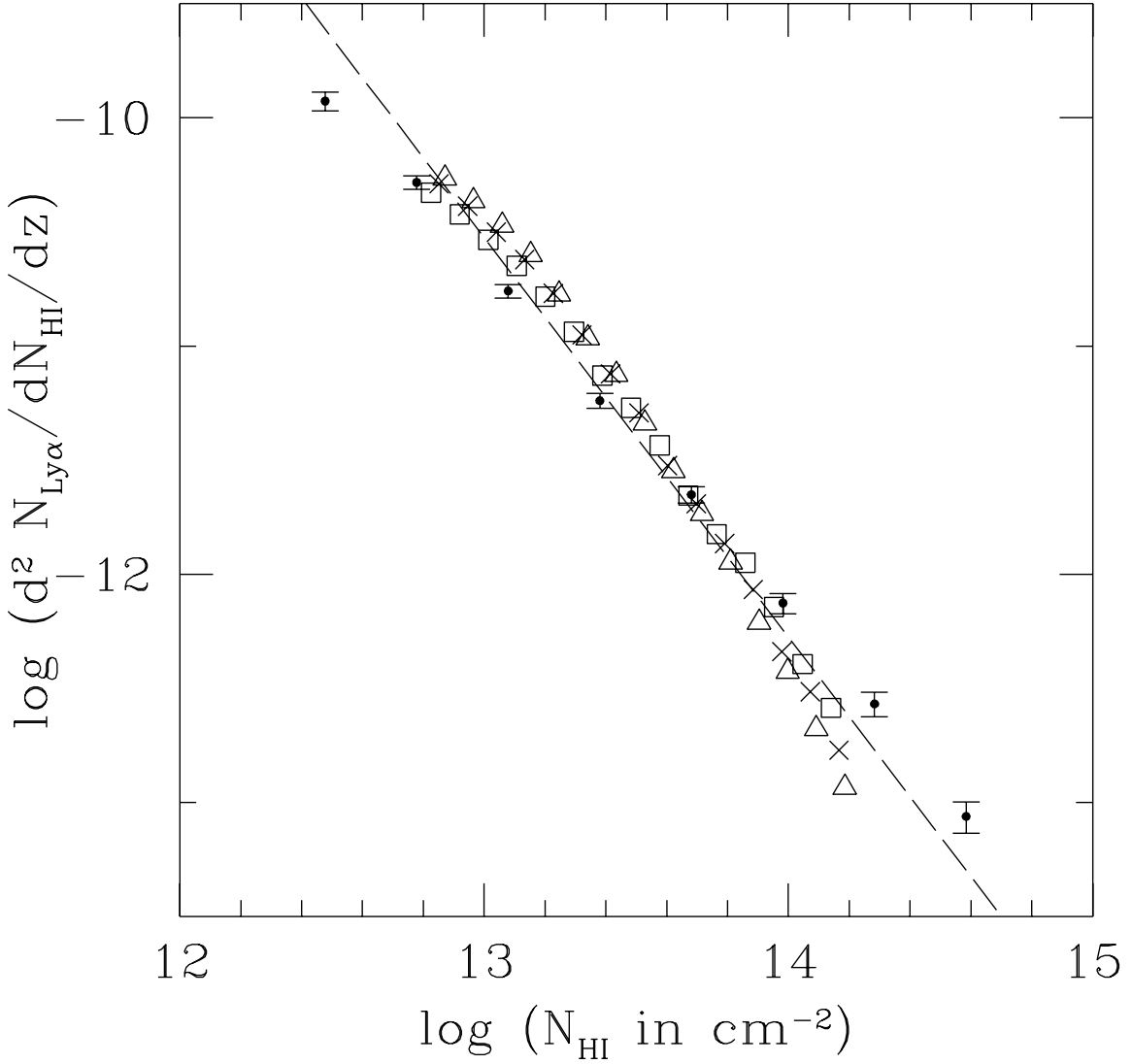


Fig. 18.— The column density distribution of the $A2$ CHDM model (Table 2) for three different values of γ (eq. [19]). $F = 2.5$ (eq. [32]) is adopted. Three values of γ are shown: $\gamma = 1.2$ (open squares), $\gamma = 1.5$ (crosses) and $\gamma = 1.7$ (open triangles). Points with error-bars are the observational data as in Fig. 7. The dashed line has a slope of $\beta = 1.75$, which is the value given in equation (41) for $\gamma = 1.2$ and σ_0 as given in Table 2.